

ABSTRACT

STUDIES OF VECTOR BOSON SCATTERING IN THE SEMILEPTONIC ZV CHANNEL WITH THE CMS DETECTOR AT $\sqrt{s} = 13$ TEV

Ramanpreet Singh, Ph.D.

Department of Physics
Northern Illinois University, 2022
Vishnu Zutshi, Director

About vector boson scattering (VBS)

NORTHERN ILLINOIS UNIVERSITY
DE KALB, ILLINOIS

SUMMER 2022

**STUDIES OF VECTOR BOSON SCATTERING IN THE SEMILEPTONIC
ZV CHANNEL WITH THE CMS DETECTOR AT $\sqrt{s} = 13$ TEV**

BY

RAMANPREET SINGH
© 2022 Ramanpreet Singh

A DISSERTATION SUBMITTED TO THE GRADUATE SCHOOL
IN PARTIAL FULFILLMENT OF THE REQUIREMENTS
FOR THE DEGREE
DOCTOR OF PHILOSOPHY

DEPARTMENT OF PHYSICS

Dissertation Director:
Vishnu Zutshi

ACKNOWLEDGEMENTS

Acknowledge people here.

DEDICATION

To my family.

TABLE OF CONTENTS

	Page
LIST OF TABLES	vii
LIST OF FIGURES	viii
LIST OF APPENDICES	x
Chapter	
1 INTRODUCTION	1
1.1 Standard model	2
1.1.1 Quantum Electrodynamics (QED)	4
1.1.2 Quantum Chromodynamics (QCD)	5
1.1.3 Electroweak Theory	6
1.1.4 Electroweak Symmetry Breaking and Higgs Mechanism	8
1.2 Vector Boson Scattering	11
1.2.1 Motivation	11
1.2.2 Topology of VBS in Semileptonic ZV Final State	13
2 THE LHC AND CMS EXPERIMENT	15
2.1 The Large Hadron Collider	15
2.1.1 Integrated Luminosity	17
2.2 The CMS Detector	18
2.2.1 The CMS Coordinate System	20
2.2.2 The Superconducting Magnet	20
2.2.3 The Tracking System	22

Chapter		Page
2.2.4	The Electromagnetic Calorimeter	23
2.2.5	The Hadronic Calorimeter	25
2.2.6	Muon Detector	26
2.2.7	Level 1 Trigger	28
3	EVENT SIMULATION AND RECONSTRUCTION	30
3.1	Track Reconstruction and Calorimeter Clustering	30
3.2	Reconstructed Particles	31
3.2.1	Muons	32
3.2.2	Electrons and Photons	33
3.2.3	Hadrons and Jets	34
3.2.3.1	N-Subjetiness and Deep Taggers	36
3.2.3.2	Softdrop Mass	38
3.2.4	Missing transverse momentum	38
3.3	TBD Monte Carlo Simulation	39
3.3.1	TBD Generators	39
3.3.2	TBD Hadronization	39
4	VBS MEASUREMENT IN ZVJJ FINAL STATE	40
4.1	TBD Signal and Background.	41
4.2	Dataset and Simulation	41
4.2.1	Data	41
4.2.2	MC Simulations	41
4.3	TBD Event Selection	46
4.3.1	TBD HLT Trigger	46

Chapter	Page
4.3.2 TBD Lepton Selection	46
4.3.2.1 TBD Muon	46
4.3.2.2 TBD Electron	46
4.3.3 TBD VBS Tagged Jets	46
4.3.4 TBD V Jet Candidate	46
5 HIGH GRANULARITY CALORIMETER UPGRADE	47
5.1 Technical Design	47
5.2 Scintillator Tiles	48
5.2.1 End of Life Scenario	48
6 TBD RESULTS	50
REFERENCES	51
APPENDICES	56

LIST OF TABLES

Table	Page
2.1 Standard physics luminosity for run-2	17
4.1 Trigger paths used to select events in CMS collision data	42
4.2 List of MC samples for Signal and Background modeling	43
4.3 List of MC samples for Signal and Background modeling	44
4.4 List of MC samples for Signal and Background modeling	45
5.1 HGCAL scenarios comparison	49

LIST OF FIGURES

Figure	Page
1.1 Standard model list of matter and interaction particles	3
1.2 3D representation of Higgs potential	10
1.3 The cross-sections for longitudinal polarized VBS involving three and four-boson coupling with and without Higgs coupling included.	12
1.4 Tree level Feynman diagram of ZV VBS process at LHC.	14
2.1 A schematic of the CERN accelerator complex.	16
2.2 Cumulative delivered and recorded luminosity versus time for 2015–2018 proton-proton collisions	17
2.3 The CMS detector cutaway view	18
2.4 The CMS detector slice view	19
2.5 The picture of the CMS detector central part when lowered in underground cavern with superconducting magnet and iron yoke visible	21
2.6 The CMS pixel upgrade.	23
2.7 The CMS ECAL schematic layout	24
2.8 The ECAL endcap quadrant assembled view	24
2.9 The first half of the barrel HCAL inserted into the superconducting solenoid (April 2006)	25
2.10 The HCAL depth segmentation after phase 1 upgrade	26
2.11 The quadrant view of CMS subdetectors layout, and the coverage of the muon detector DTs, CSCs, and RPCs highlighted	27
3.1 Comparison of τ_{21} and τ_{32} shapes for signal and background in AK8 jets . . .	37

Figure	Page
3.2 The network architecture of DeepAK8	37
5.1 Overview of CE	47
5.2 HGCAL scenarios	48

LIST OF APPENDICES

Appendix	Page
A MACHINE LEARNING	56
B DATA ANALYSIS	58

CHAPTER 1

INTRODUCTION

It doesn't matter how beautiful your theory is, it doesn't matter how smart you are.

If it doesn't agree with experiment, it's wrong. In that simple statement is the key to science.

— Richard P. Feynman

“Particle Physics” is the branch of physics which deals with the fundamental particles and the interactions between them. Fundamental particles are the subatomic particles which are not made of other particles. There are two types of fundamental particles “matter” and “interaction” particles, as the name suggests matter particles are the fundamental constituent of matter and the interactions between among them is governed by how they exchange interaction particles. Standard Model (SM) of particle physics is the theory that classifies these fundamental particles and describes three out of four fundamental interaction forces; electromagnetic, weak, and strong.

This chapter introduces briefly to the theory of SM, Higgs mechanism, spontaneous electroweak symmetry breaking (EWSB), vector boson scattering (VBS), and the motivation for the search of VBS in semileptonic decay channel ZV with leptonic decay of Z, and hadronic decay of V (W/Z) to pair of quarks.

1.1 Standard model

In SM, the matter particles are fermions, and the interaction particles are bosons. SM also includes anti-fermions, which are fermions with equal mass but opposite sign of charge. Figure 1.1 lists mass, electric charge, and spin of fermions and bosons in SM.

Fermions obey Fermi-Dirac statistics and have half integer spin. They can be further divided into leptons which have integral electric charge, and quarks which have fractional electric charge. There are three generations of quarks and leptons discovered to the date, each generation only differs by the mass. In addition to the electric charge, quarks also have three types of “color” charge (red, green and blue). Quarks cannot be isolated because of “color confinement”, which requires net color charge to be zero for an isolated particle, for this reason we can only have certain composition of quarks. Baryons (proton, neutrons, etc.) are made up of three quarks with each with different color charge, and mesons (pions, kaons, etc.) are made of two quarks with color and anti-color charge.

Bosons obey Bose-Einstein statistics and have integral spin. They are described by local gauge theory and are also called gauge boson. Photons are the interaction particle of electromagnetic force, they are massless and only interact with charged particles. Gluons are the mediator of strong force between quarks, they are massless and carries color charge. W^\pm and Z are the vector bosons and mediator of weak force, unlike photons and gluons they are massive. W^+ and W^- are antiparticles of each other, and Z is antiparticle of its own. The last gauge boson Higgs is a massive scalar boson with zero spin, zero electric and color charge. Higgs boson is not a force carrier, but rather explains why only some particles have mass.

The SM is built in the framework of quantum field theory (QFT), in which particles are excitation of the fields and interactions arise from local gauge invariance. The SM is a

$SU(3)_C \otimes SU(2)_L \otimes U(1)_Y$ gauge theory, $U(1)_Y$, $SU(2)_L$, $SU(3)_C$ are the gauge symmetries of quantum electrodynamics (QED), weak interaction and quantum chromodynamics (QCD) respectively, where the indices stands for “hypercharge” (Y), “left-handed” (L) and “color” (C).

Standard Model of Elementary Particles

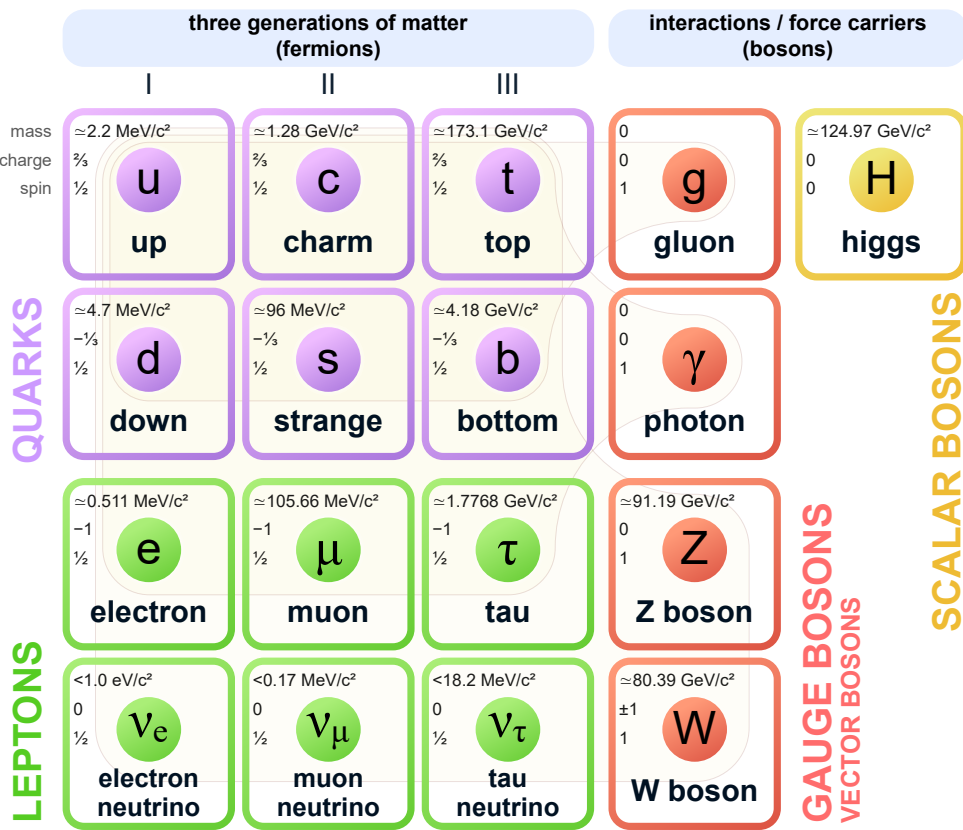


Figure 1.1: Standard model list of matter and interaction particles [1]

1.1.1 Quantum Electrodynamics (QED)

QED is a quantum field theory of electrodynamics, it describes the interaction of photons to the charged fermions. The QED is local gauge invariant and symmetric with $U(1)_Q$ group, defined as,

$$U(1)_Q = \exp(iQ\theta(x)) \quad (1.1)$$

where $\theta(x)$ is any spacetime function also called gauge parameter, and Q is coupling constant of photon field to the fermions which is equivalent to the charge of fermion.

Under this transformation, fermion spinor $\psi(x)$ and four-potential A_μ electromagnetic tensor will transform as,

$$\psi(x) \rightarrow U(1)_Q \psi(x) \quad (1.2)$$

$$A_\mu \rightarrow A_\mu - \frac{1}{e} \partial_\mu \theta \quad (1.3)$$

The general Lagrangian of QED for fermions and their interaction with photon field is given by,

$$\mathcal{L}_{QED} = \bar{\psi}(i\gamma^\mu D_\mu - m)\psi - \frac{1}{4}F_{\mu\nu}F^{\mu\nu} \quad (1.4)$$

where m is the mass of fermion, D_μ is the covariant derivative, and $F_{\mu\nu}$ is the electromagnetic field tensor defined as,

$$D_\mu = \partial_\mu + iQA_\mu \quad (1.5)$$

$$F_{\mu\nu} = \partial_\mu A_\nu - \partial_\nu A_\mu \quad (1.6)$$

1.1.2 Quantum Chromodynamics (QCD)

The strong interactions are represented by $SU(3)_C$ gauge group, invariant under transformations of color charge degree of freedom, and it is based on Yang-Mills theory [2]. Since “electrodynamics” is the theory of electric charge, this theory of color (*chromo* in Greek) charge is called “chromodynamics”, hence the name quantum chromodynamics (QCD).

A quark spinor in initial state can be represented as,

$$\psi = \begin{pmatrix} \psi_{red} \\ \psi_{blue} \\ \psi_{green} \end{pmatrix} = \begin{pmatrix} \psi_1 \\ \psi_2 \\ \psi_3 \end{pmatrix} \quad (1.7)$$

$SU(3)_C$ is an exact symmetry, it means the difference between colors cannot be measured experimentally, thus the color labels in quark spinor are arbitrary. $SU(3)_C$ transformation is defined as,

$$SU(3)_C = \exp \left(i\theta^a(x) \frac{\lambda^a}{2} \right) \quad (1.8)$$

where λ^a for $a = 1, \dots, 8$, are the Gell-Mann matrices, and $\theta^a(x)$ are any gauge parameters. These eight generators of symmetry corresponds to eight gauge vector boson gluons.

Similar to QED, the covariant derivative for QCD can be formed as,

$$D_\mu = \partial_\mu + ig_s \frac{\lambda^a}{2} G_\mu^a \quad (1.9)$$

where g_s is the coupling constant of gluon to the quarks, and G_μ^a are the eight gauge fields corresponding to gluons.

Now the corresponding field strength tensor in QCD can be formed as,

$$F_{\mu\nu}^a = \partial_\mu G_\nu^a - \partial_\nu G_\mu^a - g_s f^{abc} G_\mu^b G_\nu^c \quad (1.10)$$

where f^{abc} are the structure constants of $SU(3)_C$ which satisfy $[\lambda^a, \lambda^b] = i f^{abc} \lambda^c$ relation.

The full Lagrangian for QCD can now be constructed as,

$$\mathcal{L}_{QCD} = \bar{\psi}^i (i\gamma^\mu D_\mu{}^{ij} - m\delta^{ij}) \psi^j - \frac{1}{4} F_{\mu\nu}^a F^{a\mu\nu} \quad (1.11)$$

for mass m , indices i and j runs from 1 to 3.

The main difference of gluon field with respect to photon field is the presence of third term in field strength tensor which allows triplet and quartic self coupling of gluons.

1.1.3 Electroweak Theory

The theory of weak interaction which changes the flavor of fermions is called quantum flavor dynamics (QFD). Since the unification of electromagnetic and weak interaction into electroweak (EW) interaction by Glashow, Weinberg, and Salam [3–5], the weak interaction is better understood in terms of EW theory.

Weak interaction only couples to left-handed fermions and it is same whether the fermion is charged or not. The underlying gauge group of EW interaction is $SU(2)_L \otimes U(1)_Y$ and has

two transformations one for the left-handed doublet L and the right handed singlet fermions ψ_R which are defined as,

$$SU(2)_L \otimes U(1)_Y = \exp \left(i\theta^a(x) \frac{\sigma^a}{2} + i\theta(x) \frac{Y}{2} \right), \quad (\text{doublet}) \quad (1.12)$$

$$= \exp \left(i\theta(x) \frac{Y}{2} \right), \quad (\text{singlet}) \quad (1.13)$$

where Y is the hypercharge (linear combination of electric charge and weak isospin component), and σ^a for $a = 1, 2, 3$ are the Pauli spin matrices generator of $SU(2)$ symmetry. Left-handed fermion L doublets are,

$$L = \begin{pmatrix} \nu_e \\ e_L \end{pmatrix}, \begin{pmatrix} \nu_\mu \\ \mu_L \end{pmatrix}, \begin{pmatrix} \nu_\tau \\ \tau_L \end{pmatrix}, \begin{pmatrix} u_L \\ d_L \end{pmatrix}, \begin{pmatrix} c_L \\ s_L \end{pmatrix}, \begin{pmatrix} t_L \\ b_L \end{pmatrix} \quad (1.14)$$

and right-handed singlets are,

$$\psi_R = e_R, \mu_R, \tau_R, u_R, d_R, c_R, s_R, t_R, b_R \quad (1.15)$$

The covariant derivative of EW is then,

$$D_\mu L = \left(\partial_\mu + ig_w \frac{\sigma^a}{2} W_\mu^a + ig \frac{Y}{2} B_\mu \right) L \quad (1.16)$$

$$D_\mu \psi_R = \left(\partial_\mu + ig \frac{Y}{2} B_\mu \right) \psi_R \quad (1.17)$$

where W_μ^a and B_μ are the gauge fields. The EW Lagrangian can now written as,

$$\mathcal{L}_{EW} = i\bar{L}\gamma^\mu D_\mu L + i\bar{\psi}_R \gamma^\mu D_\mu \psi_R - \frac{1}{4} W_{\mu\nu}^a W^{a\mu\nu} - \frac{1}{4} B_{\mu\nu} B^{\mu\nu} \quad (1.18)$$

where $B_{\mu\nu}$ and $W_{\mu\nu}^a$ are fields strength, defined as,

$$B_{\mu\nu} = \partial_\mu B_\nu - \partial_\nu B_\mu \quad (1.19)$$

$$W_{\mu\nu}^a = \partial_\mu W_\nu^a - \partial_\nu W_\mu^a - g_w \epsilon^{abc} W_\mu^b W_\nu^c \quad (1.20)$$

the linear combination of B_μ and W_μ gauge field, with a weak mixing angle θ_w gives 4 vectors boson W^+ , W^- , Z , and γ of SM,

$$W_\mu^\pm = \frac{1}{\sqrt{2}} (W_\mu^1 \mp W_\mu^2) \quad (1.21)$$

$$Z_\mu = \cos \theta_w W_\mu^3 - \sin \theta_w B_\mu \quad (1.22)$$

$$A_\mu = \sin \theta_w W_\mu^3 + \cos \theta_w B_\mu \quad (1.23)$$

$$\tan \theta_w = g/g_w \quad (1.24)$$

Similar to QCD, the presence of third term in field strength tensor allows the self triple (WWZ , $WW\gamma$) and quartic ($WWWW$, $WWZZ$, $WWZ\gamma$, $WW\gamma\gamma$) couplings.

1.1.4 Electroweak Symmetry Breaking and Higgs Mechanism

The *spontaneous symmetry breaking* is the phenomena which explains why the ground state is not invariant under the symmetry of the Lagrangian. The “spontaneous” means the symmetry breaking is not done by external agent but rather by Lagrangian itself in ground state.

The EW theory unifies weak interaction and QED but the gauge boson in EW theory are all massless, if we were to add mass terms like $-m^2 W_\mu W^\mu$ by hand, it will no longer be gauge invariant. The solution to this without breaking gauge invariance is spontaneous

symmetry breaking, but this requires addition of new scalar field called Higgs field via Brout–Englert–Higgs mechanism (BEH) [6, 7], and this symmetry breaking is known as electroweak symmetry breaking (EWSB).

BEH introduces a complex scalar field as $SU(2)_L$ doublet with non-zero vacuum expectation value (VEV),

$$\phi = \begin{pmatrix} \phi^+ \\ \phi^0 \end{pmatrix} = \frac{1}{\sqrt{2}} \begin{pmatrix} \phi^1 + i\phi^2 \\ \phi^3 + i\phi^3 \end{pmatrix} \quad (1.25)$$

and BEH Lagrangian is,

$$\mathcal{L}_{BEH} = |D_\mu \phi|^2 - V(\phi) \quad (1.26)$$

where D_μ is same as EW covariant derivate in Equation 1.16, and $V(\phi)$ is,

$$V(\phi) = \mu^2 |\phi|^2 + \lambda(|\phi|^2)^2 \quad (1.27)$$

the parameter λ is required to be positive, for $\mu^2 > 0$ the minima is at 0, which is not an interesting case, but for $\mu^2 < 0$ vacuum state energy is given by,

$$\phi^\dagger \phi = -\frac{\mu^2}{2\lambda} \quad (1.28)$$

by the choice of non-zero VEV v , scalar field can be parameterized as,

$$v = \sqrt{\frac{-\mu^2}{\lambda}} \quad (1.29)$$

$$\phi(x) = \frac{1}{\sqrt{2}} \begin{pmatrix} 0 \\ h(x) + v \end{pmatrix} \quad (1.30)$$

where $h(x)$ is the Higgs field and BEH spontaneously breaks electroweak symmetry,

$$SU(2)_L \otimes U(1)_Y \rightarrow U(1)_{EM} \quad (1.31)$$

Visually the Higgs potential is shown in Figure 1.2. The ball position at the center represents unbroken symmetry, and at the minima represents spontaneous broken symmetry in the ground state of potential.

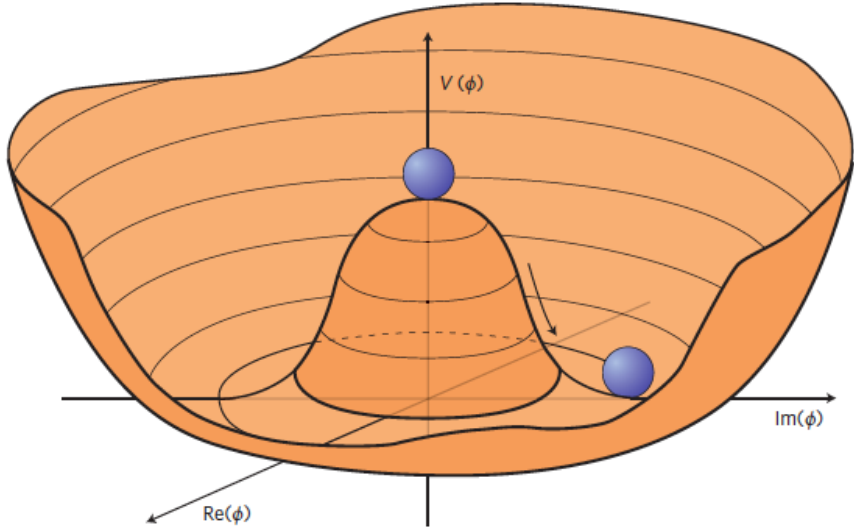


Figure 1.2: 3D representation Higgs potential [8].

After EWSB, the BEH Lagrangian contains the following mass terms,

$$m_W^2 W_\mu^+ W^{-\mu}, \quad m^2 Z Z_\mu Z^\mu, \quad m^2 h^2 \quad (1.32)$$

and gauge fields,

$$-\frac{1}{4} A_{\mu\nu} A^{\mu\nu}, \quad -\frac{1}{4} W_{\mu\nu}^+ W^{-\mu\nu}, \quad -\frac{1}{4} Z_{\mu\nu} Z^{\mu\nu}, \quad -\frac{1}{4} (\partial_\mu h)(\partial^\mu h) \quad (1.33)$$

thus explaining existence of three massive vector boson (W^\pm , Z), one massless vector boson (γ), and one massive scalar boson Higgs (H).

With experimentally measured value of VEV v approximately 246 GeV, The masses of bosons can be written in terms of v as,

$$m_A = 0, \quad m_W = \frac{g_W v}{2}, \quad m_Z = \frac{\sqrt{g_W^2 + g^2} v}{2}, \quad m_H = \sqrt{2\lambda} v \quad (1.34)$$

1.2 Vector Boson Scattering

The vector boson scattering (VBS) is,

$$VV \rightarrow VV \quad (1.35)$$

that is, when you have two vector bosons in initial state and two vector bosons in final state.

This section describes the motivation behind studying VBS, and the topology of scattering studied in this dissertation.

1.2.1 Motivation

A massless spin-1 boson can exists in two transverse polarization as,

$$\varepsilon_\pm^\mu = \mp \frac{1}{\sqrt{2}} (0, 1, \pm i, 0) \quad (1.36)$$

and massive vector bosons can also exists in one longitudinal polarization,

$$\varepsilon_L^\mu = \frac{1}{m}(p_z, 0, 0, E) \quad (1.37)$$

This means the longitudinal polarized VBS will scale as E/m , whereas the scattering of transverse polarized boson remains constant. The Figure 1.3 shows the cross-section of longitudinal polarized VBS $V_L V_L \rightarrow V_L V_L$ for low to high energies. Perturbatively the cross-section of longitudinal polarized VBS will scale with center of mass energy \sqrt{s} and eventually the unitarity is violated at ≈ 1.2 TeV scale [9, 10]. The Figure 1.3 also shows how the existence of light Higgs boson and inclusion of Higgs to vector boson coupling diagrams in longitudinal polarized VBS can restore unitarity violation, and since the discovery of Higgs boson $m_H = 125$ GeV in July 2012, the VBS studies became important and complementary to direct measurement of Higgs coupling in SM, and test for EWSB at TeV scale.

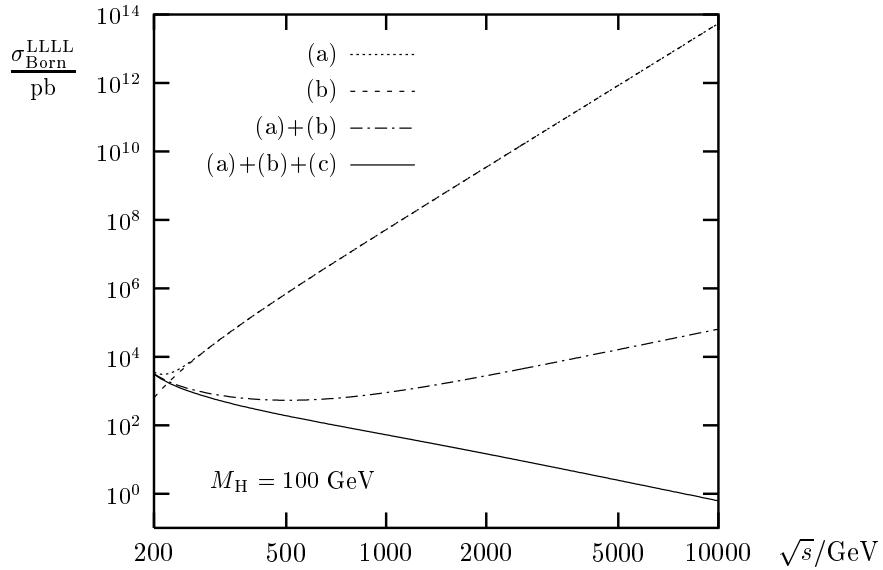


Figure 1.3: The cross-sections for longitudinal polarized VBS involving three and four-boson coupling with and without Higgs coupling diagram included. (a) is for the diagrams with three-boson coupling, (b) is for diagrams with four-boson coupling, and (c) is for diagrams with Higgs to vector boson coupling. [11]

1.2.2 Topology of VBS in Semileptonic ZV Final State

In proton-proton collisions, the actual interaction happens with the constituent quarks. For VBS to happen, the incoming (colliding) quarks have to radiate vector boson, then the scattering process between those vector boson can proceed via exchange of vector boson, Higgs boson, or quartic coupling. The tree level Feynman diagram of a VBS process in proton-proton collision is shown in Figure 1.4.

The outgoing quarks are the signature of VBS in hadron collider experiments because they will have large pseudorapidity difference between them, and will also have large invariant mass of outgoing quark pair. Generally the jets coming from these outgoing quarks are first tagged as “VBS Jets” to filter out most of the QCD background.

The type of leptonically decaying vector boson can be determined, i.e. whether it was W or Z, but for the hadronically decaying vector boson it is challenging and generally denoted by V. This analysis looks for the VBS signature with ZV in final state with Z decaying to two opposite sign same flavor (OSSF) leptons, and V decaying to pair of quarks.

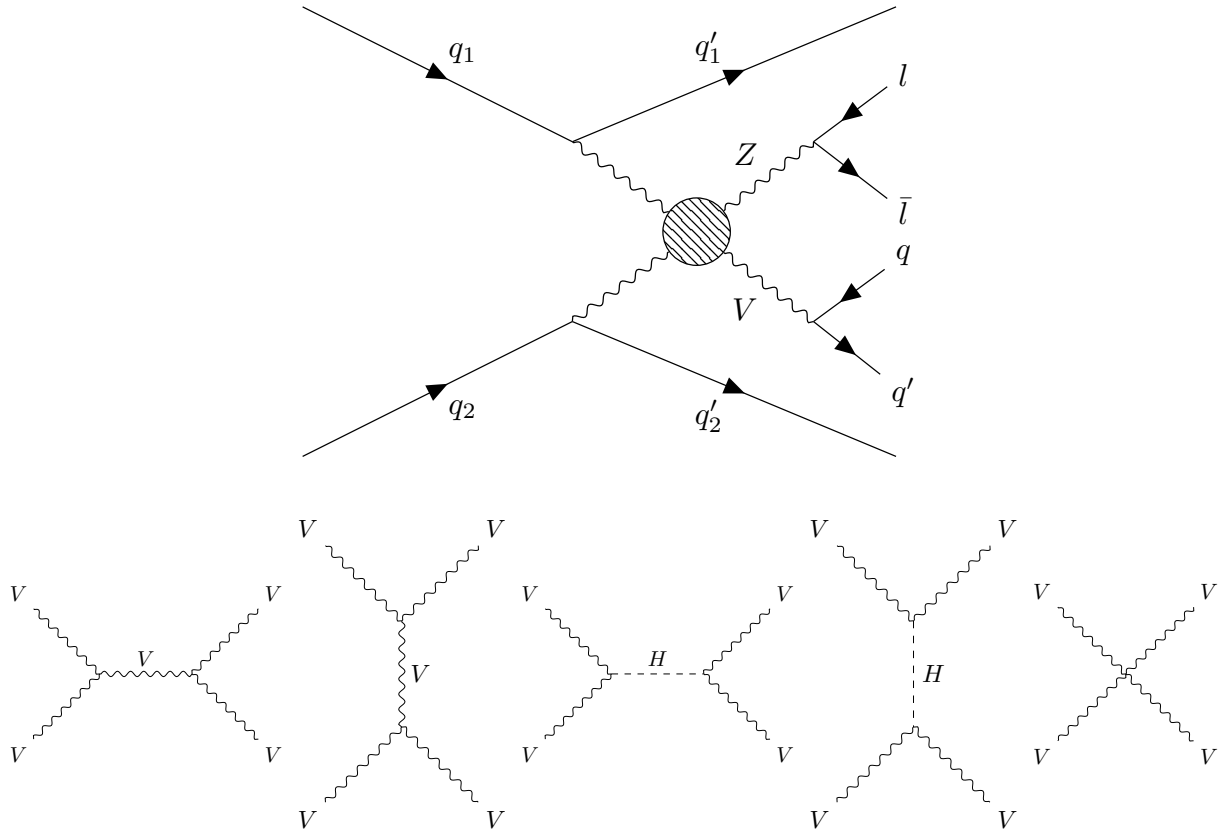


Figure 1.4: Tree level Feynman diagram of ZV VBS process at LHC. The top diagram shows the production of two vector bosons being radiated from incoming quarks, in final state after scattering (blob), Z decays to pair of leptons, V (W/Z) decays to pair of quarks, and plus two outgoing quarks. The bottom row of diagram shows the tree level processes that can happen in scattering represented by blob in top diagram, starting from s and t-channel exchange of vector boson, Higgs boson, and the last one is quartic coupling of vector bosons.

CHAPTER 2

THE LHC AND CMS EXPERIMENT

The physics analysis is carried out using Compact Muon Solenoid (CMS) experiment at European Council for Nuclear Research (CERN) Large Hadron Collider (LHC) accelerator. This chapter provides overview of LHC and detail of CMS experiment and its sub-detectors for particle tracking and calorimetry.

2.1 The Large Hadron Collider

The LHC is the largest accelerator located at CERN in Geneva, Switzerland. The main LHC ring is 27 km in circumference and around 50 to 175 m underground. The LHC is built to collide protons at 14 TeV center-of-mass energy, LHC delivered proton-proton collisions at 7 and 8 TeV during run-1 (2010–2012), and at 13 TeV center-of-mass energy during run-2 (2015–2018) [12].

The Figure 2.1 describes CERN accelerator complex. The protons are sourced by ionizing hydrogen atoms and then fed into linear accelerator (LINAC). The LINAC accelerates the protons to 50 MeV and sent to the booster. Then the booster increases energy of protons to 1.4 GeV and feeds it to the proton syncrotron (PS) which further increases energy to 25 GeV and starts bunching them together with bunches 25 ns apart. Then the proton bunches are passed through super proton synchrotron (SPS) which increases energy to 450 GeV and finally sent to main LHC clockwise and counterclockwise rings where they are accelerated to

final energy required which is 6.5 TeV for both bunches going clockwise and counterclockwise to obtain collisions at 13 TeV center-of-mass energy.

The proton-proton collisions occurs at four different location where two general purpose detectors CMS and A Toroidal LHC Apparatus (ATLAS), and two specific purpose detector A Large Ion Collider Experiment (ALICE) and LHC-beauty (LHCb) are located.

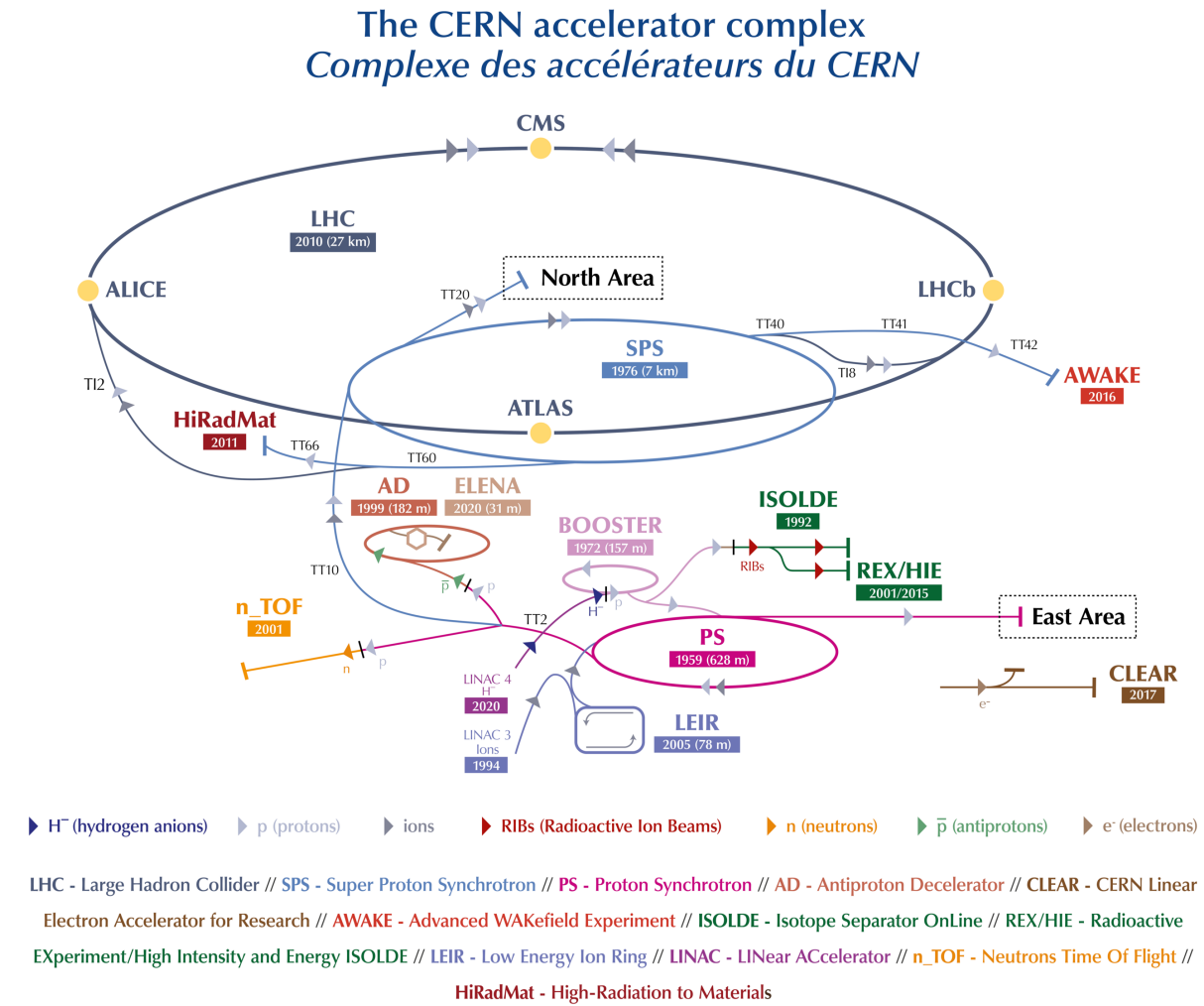


Figure 2.1: A schematic of the CERN accelerator complex [13]

2.1.1 Integrated Luminosity

The number of events generated in a collisions for a given process is,

$$N = L\sigma \quad (2.1)$$

where σ is cross-section of the process and L is the luminosity of the LHC.

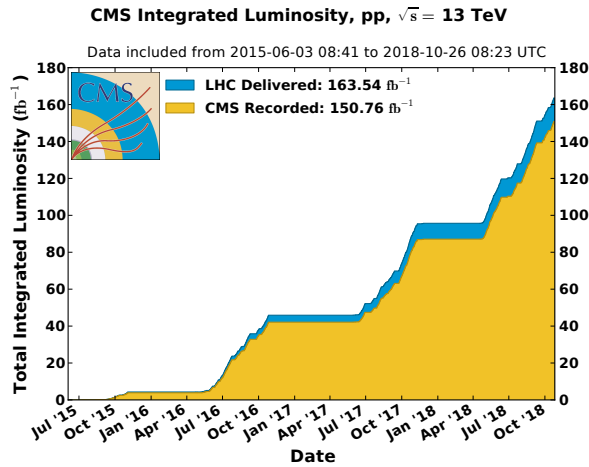


Figure 2.2: Cumulative delivered and recorded luminosity versus time for 2015–2018 proton-proton collisions [14]

Cumulative luminosity delivered and recorded by CMS during run-2 operation is shown in Figure 2.2. For run-2 standard physics analysis luminosity recorded during 2016–2018 is considered, and only runs certified as “golden” by CMS Luminosity physics object group (POG) for analysis are used. The total luminosity for run-2 standard physics is 137.19 fb^{-1} and separately for years in Table 2.1 [15–17].

Table 2.1: Standard physics luminosity for run-2

2016	2017	2018	run-2
35.92 fb^{-1}	41.53 fb^{-1}	59.74 fb^{-1}	137.19 fb^{-1}

2.2 The CMS Detector

The CMS detector is a general purpose detector. A cutaway view of the detector is shown in Figure 2.3. The detector is cylindrical with dimensions 21 meters long, and 15 meters in diameter, and the whole detector weighs about 14000 tonnes. The detector is built in slices with central region called “barrel”, and two closing end sides called “endcap”. A superconducting solenoid generates magnetic field of 3.8 T inside and 2 T outside, and to contain the magnetic field outside of solenoid and support structure of the detector massive steel yokes are used.

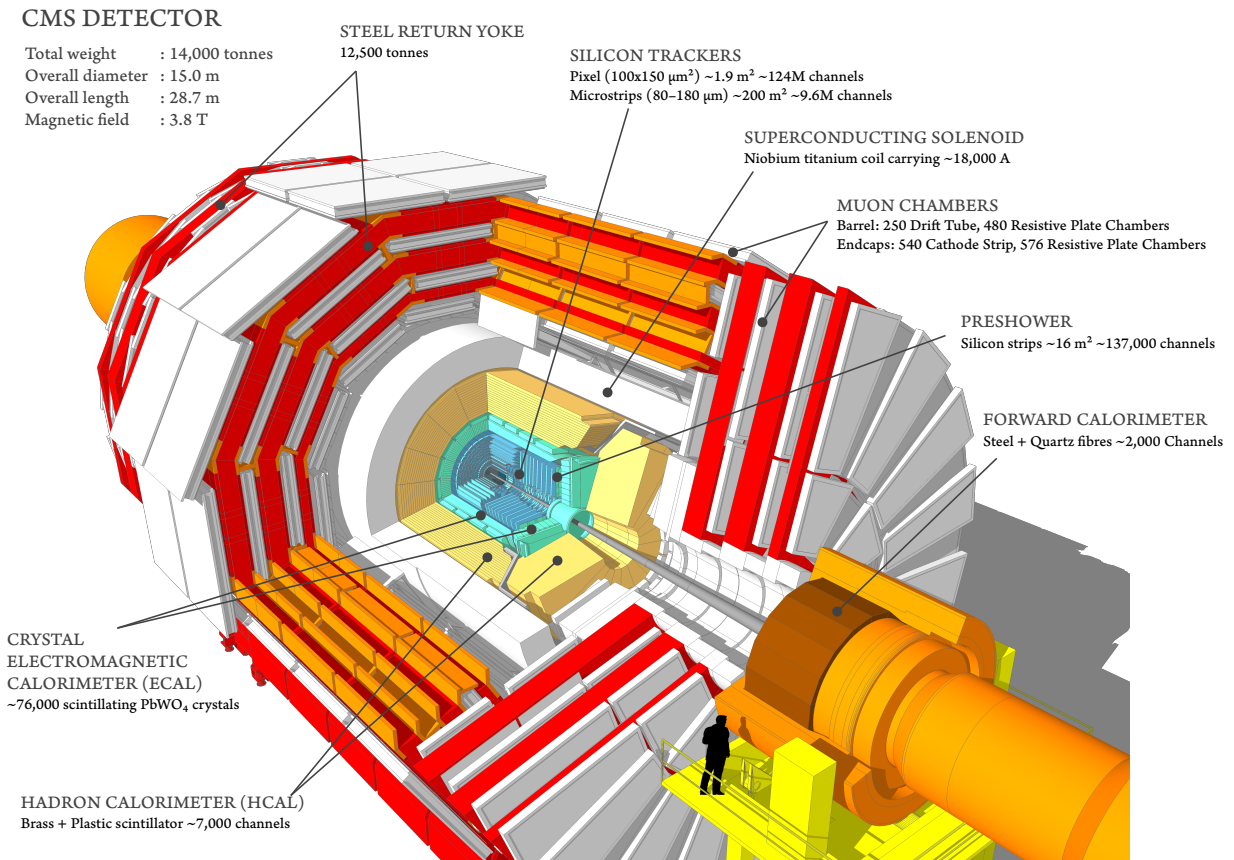


Figure 2.3: The CMS detector cutaway view [18]

The slice view of CMS in Figure 2.4 shows how different particles leave signature in CMS detector. Neutral particles such photons, neutrinos, and hadrons will leave no track in Silicon Tracker (ST), and are identified by only energy deposited or missing energy. Electrons are identified from the track in ST and energy deposit in Electromagnetic Calorimeter (ECAL), hadrons are heavier and they pass through ECAL and deposit their energy completely in Hadronic Calorimeter (HCAL), leaving only small fraction of energy in ECAL. Since muons are minimum ionizing particle (MIP), they pass through whole detector with very small fraction of energy deposit in ECAL and HCAL.

This section describes the subsystems of CMS detector. For detailed technical description refer to [19].

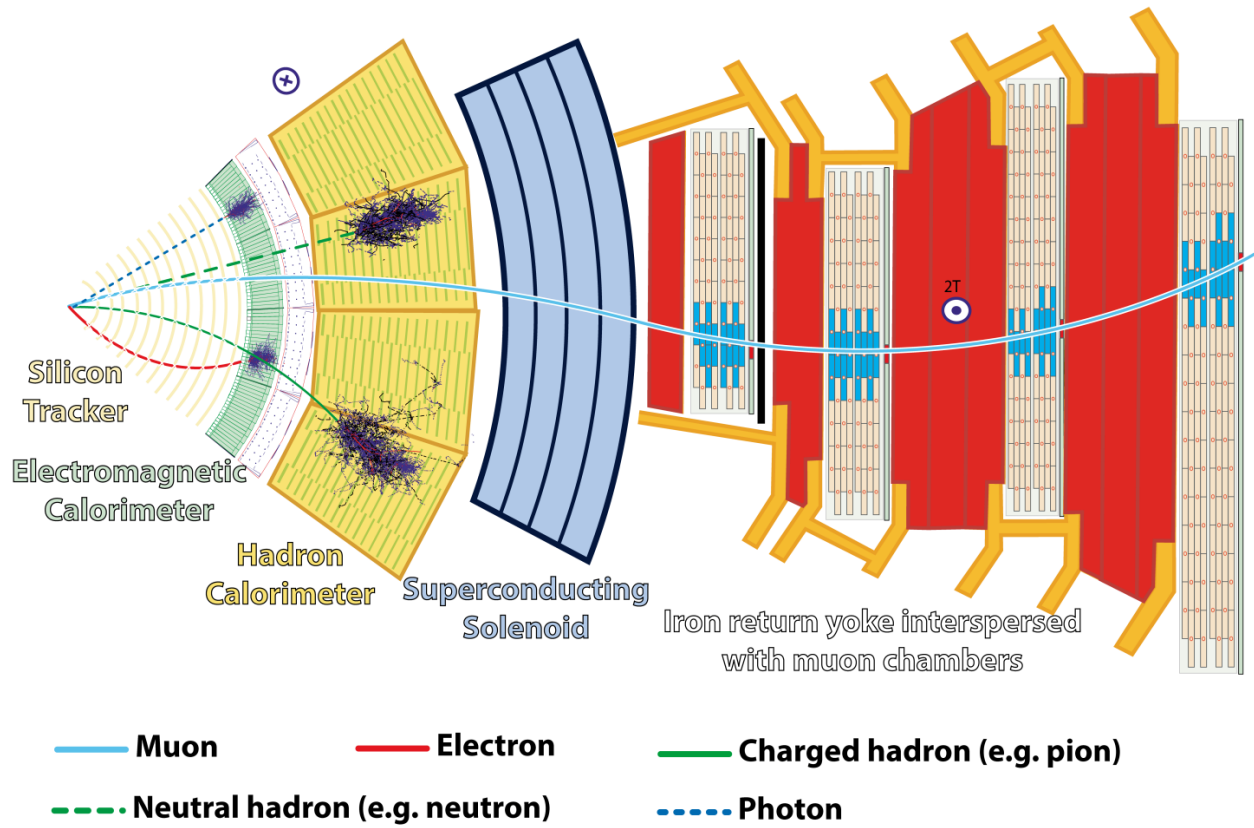


Figure 2.4: The CMS detector slice view [20]

2.2.1 The CMS Coordinate System

CMS uses interaction point (IP) of collisions as origin to define right-handed coordinate system. The z -axis is along the beamline, the x -axis points toward the center of the LHC, and the y -axis points upwards, toward Earth's surface. The transverse plane $x - y$ is used as to calculate most commonly used quantities like transverse momentum p_T and energy E_T .

To describe the direction of particles leaving the IP, azimuthal ϕ and polar θ angles are used. ϕ is measured around the beam axis, and θ is measured from the beam axis. In collider physics, pseudorapidity η (Lorentz invariant) is used to describe direction from beam pipe instead of θ as,

$$\eta = -\ln[\tan \theta/2] \quad (2.2)$$

and sometimes in terms of rapidity y as,

$$y = \frac{1}{2} \ln \frac{E + p_z}{E - p_z} \quad (2.3)$$

Particles kinematics can be completely described in terms of p_T , η , ϕ , and E_T or mass. The distance between the two particles ΔR in $\eta - \phi$ plane is described as,

$$\Delta R = \sqrt{(\Delta\eta)^2 + (\Delta\phi)^2} \quad (2.4)$$

2.2.2 The Superconducting Magnet

The superconducting magnet is the main part of the CMS detector, it is 12.5 meters long and 6.3 meters in diameter. The magnet is cooled to 4.5 K and 20 kA current flows through it to generate 3.8 T of magnetic field with stored energy of 2.6 GJ.

The Figure 2.5 shows visible superconducting magnet and iron yoke when part of CMS detector was lowered in the underground cavern during installation in 2007.

The key purpose of magnet is to determine the momentum and the sign of charged particles by bending them. The momentum resolution of the particles will decrease with increase in p_T , with constant 3.8 T magnetic field inside and it has momentum resolution of $\Delta p/p \approx 10\%$, which is enough to determine unambiguously the sign of muons with momentum of $\approx 1 \text{ TeV}/c$.

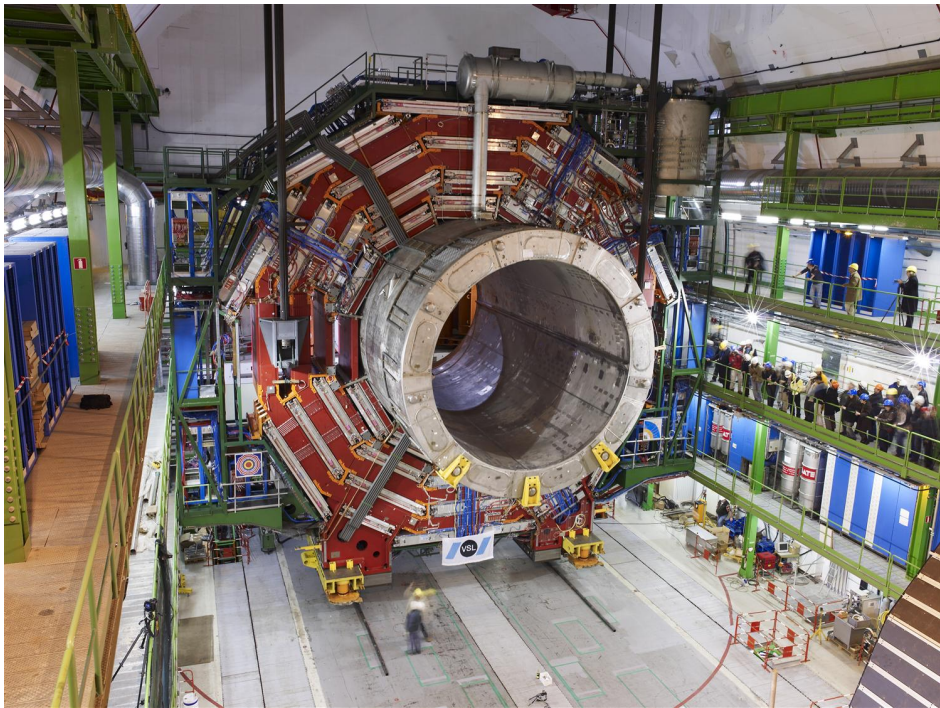


Figure 2.5: The picture of the CMS detector central part when lowered in underground cavern with superconducting magnet and iron yoke visible [21].

2.2.3 The Tracking System

The CMS tracking system ST is the innermost part of the detector, it is made up of pixel and strip detectors. The main goal of ST is to reconstruct the tracks of the charged particles with high precision in high pileup environment.

Silicon is most commonly used material for making tracking systems because of it's semiconductor properties, and high radiation hardness which is essential for the innermost detector. When a p-n junction is built on silicon substrate it creates a depletion zone with no charge carriers at the junction, and whenever a charged particle pass through the depletion zone it creates a electron-hole pair, and under reverse bias this electron-hole generates electrical signal. The CMS tracking consists of about 124 million channels of such junctions in pixel detector and 10 million in strip detector.

The pixel detector was upgraded in 2017 and the comparison of layers before and after the upgrade is shown in Figure 2.6. It is made up of four barrel layers and three endcaps, with nearest barrel layer being 3 cm away from beamline for precise measurement of IP. Because of the large number of pixel channels, the readout is done by Application-specific integrated circuits (ASICs).

The outermost part of ST detector is made of silicon strips. It allows large coverage by reducing number of readout channels. It has 10 layers in barrel region and 12 discs in endcap region. For better signal-to-noise ratio and radiation tolerance both pixel and strip operates at -20 °C.

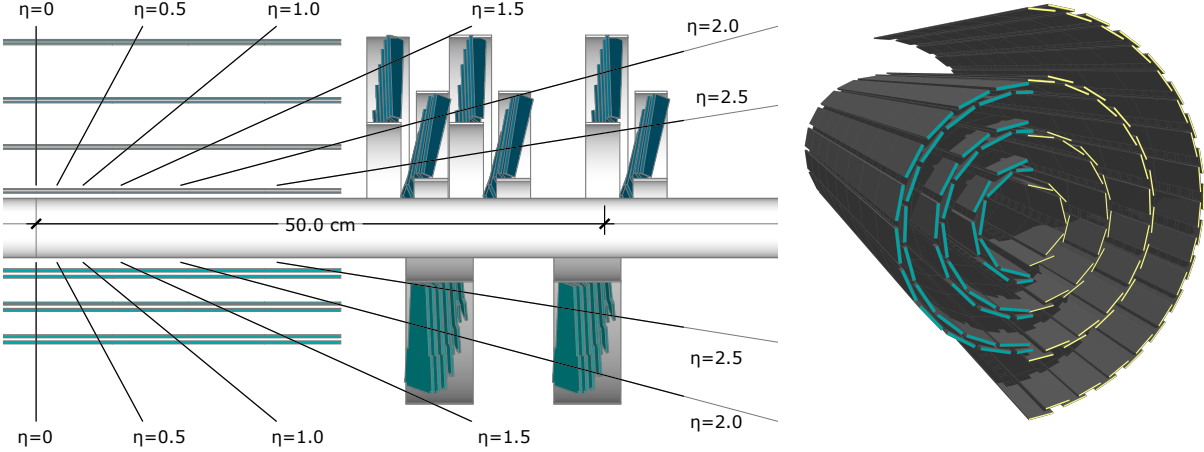


Figure 2.6: The CMS pixel upgrade. The left is cross sectional view of pixel detector layers before upgrade (bottom) and after Phase 1 upgrade (top). The right is view pixel barrel before upgrade (left) and after upgrade (right) [22].

2.2.4 The Electromagnetic Calorimeter

The ECAL active material is made of lead tungstate (PbWO_4) scintillating crystals and two layers silicon strip for preshower in front of the endcaps. The crystals in central barrel section are mounted in quasi-projective geometry pointing towards IP and covers $|\eta| < 1.48$, and two endcaps extends the coverage to $|\eta| = 3.0$. The schematic layout of ECAL is shown in Figure 2.7 and the picture of endcap quadrant when assembled in Figure 2.8

The main purpose of ECAL is to determine energy and positions of electromagnetically interacting particles. To determine particle need to completely deposit their energy, except electron and photons all other particles pass through ECAL crystals with only small fraction of energy signature in crystals. When electron and photon interacts with PbWO_4 it starts the process of electromagnetic shower and continues until the energy the energy of the incident particle is below threshold, which is about 1 MeV.

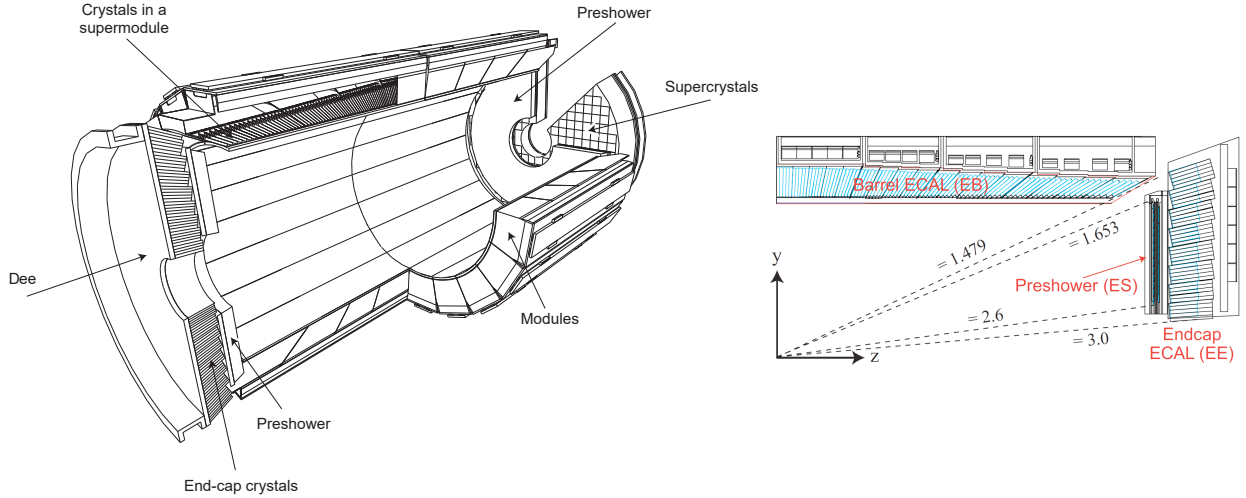


Figure 2.7: The CMS ECAL schematic layout. The left is schematic showing arrangement of superclusters in barrel and endcap (with preshower layers). The right is $y - z$ plane quarter view of ECAL layout [23].

The resolution of the ECAL energy measurements can be described as,

$$\left(\frac{\sigma}{E}\right)^2 = \left(\frac{S}{\sqrt{E}}\right)^2 + \left(\frac{N}{E}\right)^2 + C^2 \quad (2.5)$$

where S is the stochastic term, N is related to the noise, and C is a constant offset.

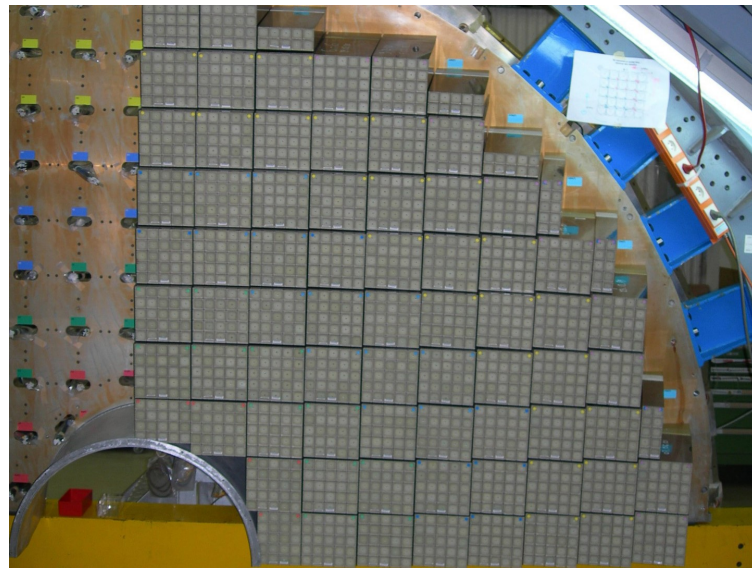


Figure 2.8: The ECAL endcap quadrant assembled view [24].

2.2.5 The Hadronic Calorimeter

HCAL is last subdetector inside solenoid after ECAL and the first half of barrel HCAL inserted is shown in Figure 2.9. Similar to ECAL the purpose of HCAL is to shower hadrons, and measure their energy and position. HCAL is made up of towers pointing towards IP and each tower is made up of sampling layers with alternating layers of plastic scintillator and brass. Brass acts as absorber in HCAL and causes hadrons to shower, then from the light output of scintillator receiving secondary shower particles gives the amount of energy deposit in each layer. In phase 1 upgrade the HCAL was upgraded to give energy deposit as function of depths and the depth segmentation schematic is show in Figure 2.10 and the details of upgrade are in technical design report [25].

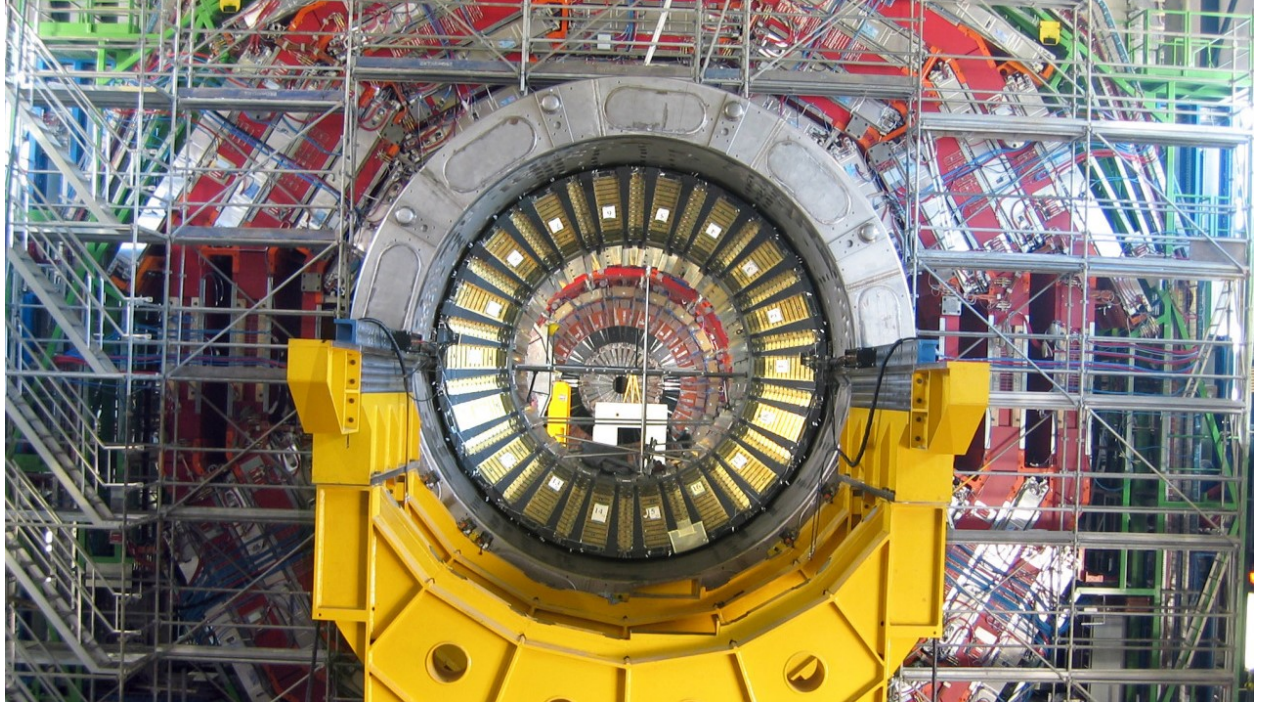


Figure 2.9: The first half of the barrel HCAL inserted into the superconducting solenoid (April 2006) [26].

HCAL consists barrel (HB) and two endcaps (HE) located inside solenoid. These two subsystems combined cover region $|\eta| = 3.0$, which is most of physics analysis done in CMS. There are two other subsystems of HCAL outside solenoid, a forward HCAL (HF) and outer barrel HCAL (HO). HO was added to ensure there is no leak from the particles that make past the solenoid. HF extends the coverage to $|\eta| = 5.0$ and is based Cherenkov radiation principle unlike other subsystems of HCAL, and it uses quartz fiber as active material with steel absorbers. HF is used most commonly used by heavy ion analysis.

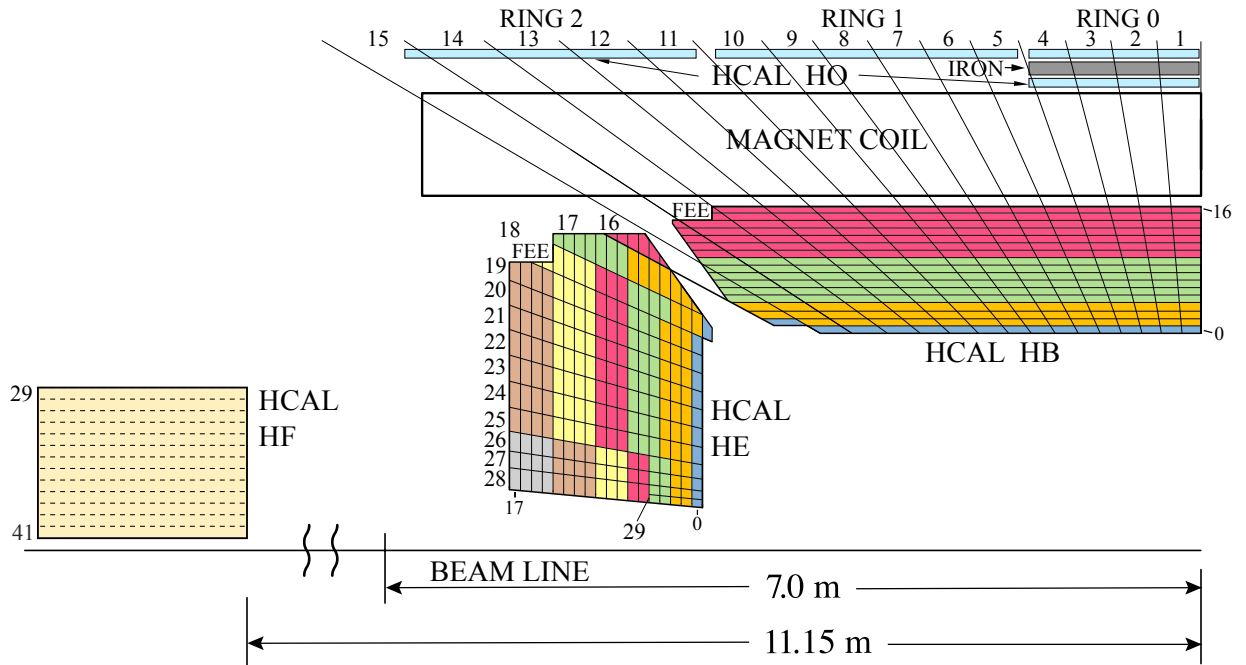


Figure 2.10: The HCAL depth segmentation after phase 1 upgrade [27].

2.2.6 Muon Detector

The outermost subsystem in the CMS detector is the muon detector. Unlike electrons, muons are MIPs, they do not lose much of their energy while passing through tracker, calorimeter and solenoid. Muon detector is build to identify, measure momentum and trigger

the events with muons. Like other subsystems, muon detector consists of barrel and endcap detector and schematic layout is highlighted in Figure 2.11.

The muon detector consists of three subsystems drift tubes (DTs), cathode strip chambers (CSCs) and resistive plate chambers (RPCs).

The DTs are wire gas detectors filled with Argon and composed of many tube cells of about 4 cm. Muon passing through these tubes ionizes Argon and free electron is detected with wires as cathode. Each DT is about 2 meters by 2.5 meters in size, and there are four layers of the DTs interleaved with iron yoke parallel to the beam pipe in barrel region. The drift time is the order of about 380 ns.

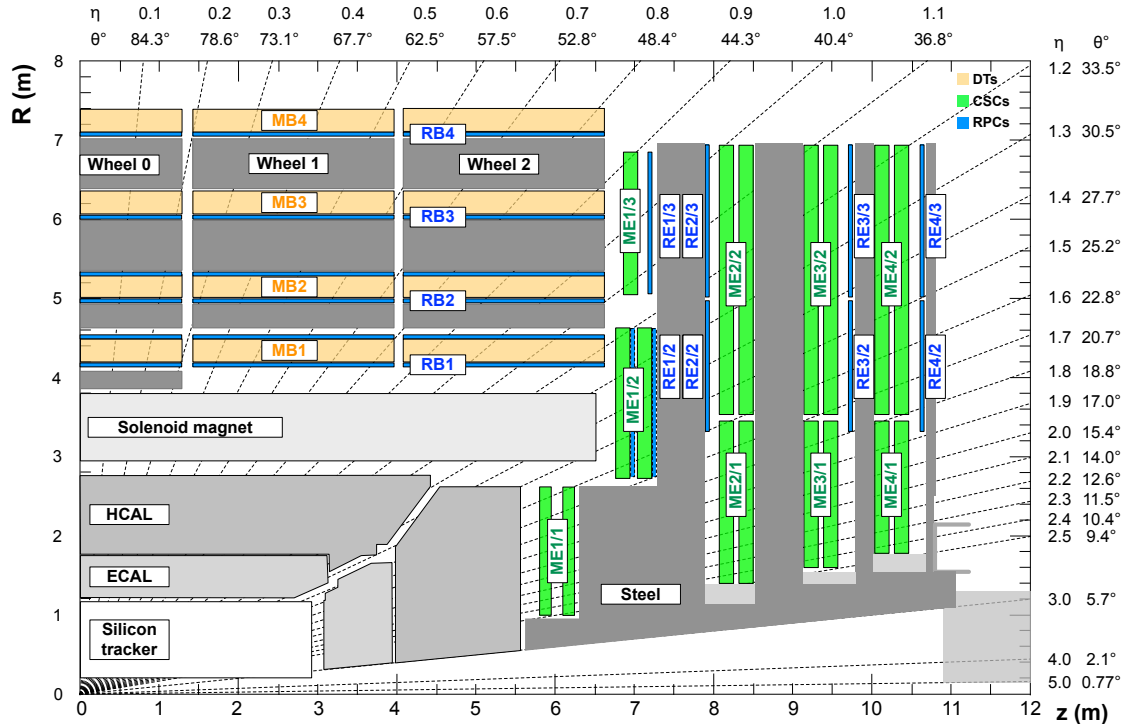


Figure 2.11: The quadrant view of CMS subdetectors layout, and the coverage of the muon detector DTs, CSCs, and RPCs highlighted [28].

The CSCs are based on same principle as DTs, and are made of multi-wire proportional chambers consisting of 6 anode planes interleaved with 7 cathode planes. They have time

resolution smaller than 5 ns. The CSCs are used in endcap region, where radiation hardness is required, and non uniform magnetic field does neutrinos effects the the measurement.

The RPCs are made up of two high resistive parallel plates, with oppositely charged plates and gas volume between them. When a charged particles passes through it and ionizes the gas, it creates an avalanche and charge is collected by metallic readout strips. RPCs have poor position resolution but fast readout of the order of 1 ns, which is fast compared to DTs, this is the reason there are 1 or 2 RPCs attached to both DTs, and CSCs.

2.2.7 Level 1 Trigger

Since proton-proton collisions happens every bunch crossing which is 25 ns apart, which is equivalent to 40 MHz collisions rate. At this collisions rate, the data storage required will be enormous and CMS can only record up to 1000 events per second. Since most of events does not contain interesting physics events, they can be thrown away. To do this CMS has two tier trigger system Level-1 Trigger (L1T), and High Level Trigger (HLT).

The L1T is the foremost electronic processing system through which event information is processed before it is passed to second trigger system HLT. The L1T is designed to make fast decisions in about $3.8\ \mu s$, and only uses ECAL, HCAL and muon system to make decision. L1T cut downs the data rate from 40 MHz to 100 kHz. The L1T electronics is placed next to the detector in underground cavern for fast transfer of data.

The HLT further reduces the data rate from 100 kHz to about 1 kHz using a computer farm with nearly 26000 cores. HLT uses all the available information from the event to make decision in about 300ms. HLT is modular by design to allow the use of information from different systems to construct multiple paths called HLT paths, for example the single muon

HLT path will save event with at least one muon passing the selection criteria set in HLT path. Events passing at least on HLT path are save for offline physics analysis.

CHAPTER 3

EVENT SIMULATION AND RECONSTRUCTION

The proton-proton collision at LHC produces shower of particles, before the event information can be easily used in an analysis, the data collected goes through iterative process of reconstruct particles produced in collision. CMS uses particle flow (PF) algorithm to reconstruct 4-vectors of muons, electrons, photons, hadrons, jets and missing transverse momentum [29].

To analyze the data collected and compare it with theoretical model, events are simulated using Monte Carlo (MC) event generators and are passed through detector simulation and PF so that MC events can be treated same as real events.

This chapter describes the basic ingredients for object reconstruction, PF candidates and MC event generators used in this analysis.

3.1 Track Reconstruction and Calorimeter Clustering

For complete particle reconstruction two main ingredients are tracks left by particle in the detector, and energy deposit in calorimeter. This section describes track reconstruction from the hits in Tracker and Muon Detector, and energy deposit measurement from calorimeter clustering.

Track reconstruction requires reconstructed hits, and seed generation which are described in [30], then the track reconstruction is done using pattern recognition which is based on combinatorial Kalman Filtering (KF) method [31]. It is an iterative process starting from

seed layer the track is estimated and then proceeds to next layer one by one, at each successive layer the track trajectory is better known. There can be multiple hits in each new layer, for this multiple trajectory candidates are created. All the trajectory candidates are grown in parallel to avoid bias, and truncated at each layer to prevent exponential increase in number of candidates. Then finally the track is fitted to compute momentum and vertex information.

The main purpose of calorimeter clustering is to determine position and energy deposit of the particle. A cluster in a calorimeter is a local group of energy deposits that are spatially consistent with a electromagnetic or hadronic shower. First the topological clusters are identified, a topological cluster is a contiguous region of energy deposit, then a seed is identified in topological cluster with certain energy threshold, and highest among the 8 neighbors for ECAL and 4 neighbors for HCAL. Now starting with seed energy and position, the neighbors energy are added, and new position is calculated. For the case when we have just one seed, there is only iteration until all the neighbors are added, in case when we have more than one seeds in a cluster, the energy from neighbors is shared, the fraction of energy shared depends on the energy and position of the cluster, after the first iteration of calculation of the energy and position the process is repeated with new values of cluster's energy and position until either the maximum iteration is reached or cluster's energy and position values are converged.

3.2 Reconstructed Particles

After tracks and calorimeter clusters are formed, PF links this information from the detectors together to form objects as broadly discussed in Section 2.2 and shown in Figure 2.4. This section describes the properties of those reconstructed particle candidates.

3.2.1 Muons

Reconstructing muon with best precision is the key ingredient for many physics searches. Muons reconstruction and identification uses all the information from tracker, calorimeters and muon detector. There are two types of reconstruction performed “Global” and “Tracker” for muon candidates. Global muons are formed combining and refitting muon hits in the muon detector with compatible track from ST, and the tracker muons are formed by extrapolating tracks from ST to segments in muon detector.

Once the muon candidates are found, the kinematics properties (p_T, η, ϕ) are calculated from track fitting, and other properties such as distance form primary vertex (PV) d_{xy}, d_z , number of hits in the tracker and muon system, tracker based relative isolation (3.1) in a cone of $\Delta R = 0.3$, and PF relative based isolation (3.2) in a cone of $\Delta R = 0.4$ are stored for cleaning and isolating muons for physics analysis.

The tracker and PF based relative isolation are defined as,

$$\text{TkIso03} = \left(\sum p_T^{\text{Tracks (PV)}} \right) / (p_T^\mu) \quad (3.1)$$

$$\text{PFRelIso04} = \left(\sum p_T^{\text{CH (PV)}} + \min \left[0, \sum E_T^{\text{NH}} + \sum E_T^\gamma - 0.5 \sum p_T^{\text{CH (PU)}} \right] \right) / (p_T^\mu) \quad (3.2)$$

where “Tracks (PV)” refers to all the tracks in tracker and coming from PV, “CH (PV)” and “CH (PU)” refers to charged hadrons coming from PV and pile up (PU) respectively, “NH” refers to neutral hadrons, μ refers to muon, and γ refers to photon.

There are multiple source of muons whenever collision event happens, they can be real muons or hadrons which are misidentified as muons, these hadrons are able “punch” through HCAL and leaves hit in muon detector. The real muons of interest are called “prompt” muons and others are either usually referred as “fake” or “non-prompt”. Fake muons can originate

from decay of pions and kaons in flight usually identified with a “kink” in track or from heavy flavor decay of b or c-quarks which are identified with tracks not originating from PV. The prompt muons are the ones coming from decay of H, W, Z bosons and τ leptons, and have small impact parameter from PV, have hits in both tracker and muon detector, and are typically well isolated.

In addition to muons from collision events, there can be cosmic muons from pion decay in upper atmosphere. Cosmic muons are generally not in-time with collision and far from interaction points.

3.2.2 Electrons and Photons

Since there is large amount of material in tracker, electrons often emit bremsstrahlung photons when passing through tracker volume, and photons can further decay to e^-e^+ pair which complicates the tracking algorithm. The energy deposit of such electrons emitting bremsstrahlung will have large spread in ϕ direction because the magnetic field will bend electrons in ϕ whereas photons are unaffected. For this reason electron and photon reconstruction are done together, and the Gaussian-sum filter (GSF) algorithm is used for electron track reconstruction which takes care of kinks in electrons track because of hard emission [32].

An electron is reconstructed when an ECAL cluster matches a GSF track, and a photon is reconstructed when an ECAL cluster with E_T more than 10 GeV is found and have no matching GSF track. To prevent electron and photon from being misidentified as jets certain conditions are applied, for electron the number of GSF track matching with ECAL cluster is limited to maximum of two, and energy deposit in a cone of $\Delta R = 0.15$ in HCAL around the position of electrons and photons is required to be less than 10%.

Similar to muons, after electron and photon reconstruction is done, their kinematics properties are calculated and various other properties required for cut based and Multivariate analysis (MVA) based identification are stored. The detailed description of electrons and photons identification technique and properties used in this dissertation can be found in Reference [33].

3.2.3 Hadrons and Jets

Quarks and gluons produced in a collision event are not detected directly, because of color confinement, they go through fragmentation and hadronization making a collimated spray of particles mostly made of hadrons and are called “jets”. Charged hadrons are reconstructed when a HCAL cluster can be associated with one or more tracks, if the track association fails the cluster is reconstructed as neutral hadron.

Jet in CMS are reconstructed using FASTJET package [34], which takes input of all PF candidates and associated tracks. The clustering basically combines 4-vectors of particles iteratively and stop when distance between two particles (d_{ij}) is higher than stopping distance (d_{iB}).

d_{ij} and d_{iB} are defined as,

$$d_{ij} = \min(p_{Ti}^{2p}, p_{Tj}^{2p}) \frac{\Delta R_{ij}^2}{R^2} \quad (3.3)$$

$$d_{iB} = p_{Ti}^{2p} \quad (3.4)$$

where p is the parameter for different clustering algorithms, R is the cone size, and ΔR_{ij} is distance between two particles in iteration.

Anti- k_T (AK) is the most use jet algorithm in physics analysis, this corresponds to $p = -1$, this means the hard particles will be clustered first in this clustering algorithm. The cone size used for standard jets (AK4) is $R = 0.4$, and for large jets (AK8) often called “fatjet” is $R = 0.8$.

To mitigate the effect of PU contamination in jets two most commonly used techniques are charged hadron subtraction (CHS) and Pileup Per Particle Identification (PUPPI) [35]. CHS as the name suggests removes all the PF in the jet clustering which are originating from PU vertices, and it is a standard technique for AK4 jets. PUPPI works by identifying PU in an event from charged PU information, then it assigns a weight to all the other particles inside jet, such as neutral particles, the weight is then used to rescale momentum of those particles. The main limitation of CHS is that it only removes charged PU contribution, for larger jets it can be issue, since it is clustering larger number of particles and can have significant contribution from neutral hadrons, for this reason PUPPI technique is used for AK8 jets.

To improve the jet selection and reject jets originating purely from PU two methods are used in this dissertation, jet identification based on multiplicities and energy fraction of particles contained in the jet, and MVA based PU identification which uses jets shape variables to discriminate prompt jet from pileup jets. The details of PU mitigation and identification used in CMS are described in Reference [36].

After jets reconstruction is complete the in addition to calculating kinematics properties (p_T , η , ϕ and mass), various other properties such as b-quark tagging and quark-gluon likelihood are also calculated and stored.

3.2.3.1 N-Subjetiness and Deep Taggers

The origin of fatjets are usually when heavy energetic particle often referred to as “boosted” decays hadronically, for example boosted W or Z bosons decaying to a pair of quarks. To find and discriminate the fatjet of interest based on its substructure the two techniques studied and used are N-Subjetiness [37] and “deep tagger” [38].

N-Subjetiness is defined as,

$$\tau_N = \frac{1}{d_0} \sum_k p_{T,k} \min\{\Delta R_{1,k}, \Delta R_{2,k}, \dots, \Delta R_{N,k}\} \quad (3.5)$$

where k runs over constituent particles in a jet, $\Delta R_{J,k}$ is the distance between subjet J and k constituent, and d_0 is the normalization constant defined as,

$$d_0 = \sum_k p_{T,k} R_0 \quad (3.6)$$

τ_N quantifies to what degree a jet can be regarded as made of N jets. The small values of the τ_N means a jet is more likely to have N or less subjets, and higher value means it will at least have $N + 1$ subjets. Rather than using τ_N alone, ratio of different τ_N variables is used, which more discriminating for cases like W vs QCD jets. Figure 3.1 shows distribution of τ_{21} and τ_{32} shapes in signal and background. τ_{21} is used to discriminate fatjets with 2-prongs (W/Z/H) and τ_{32} with 3-prongs (t-quark) substructure against QCD jets.

Deep Tagger for AK8 are Machine learning (ML) based tagger developed to determine origin of a fatjet. These taggers are trained on particle level information from PF and provide multi class tagging probabilities. In addition to there are versions of these taggers which is de-correlated from the mass of jet, this is important for analysis including this

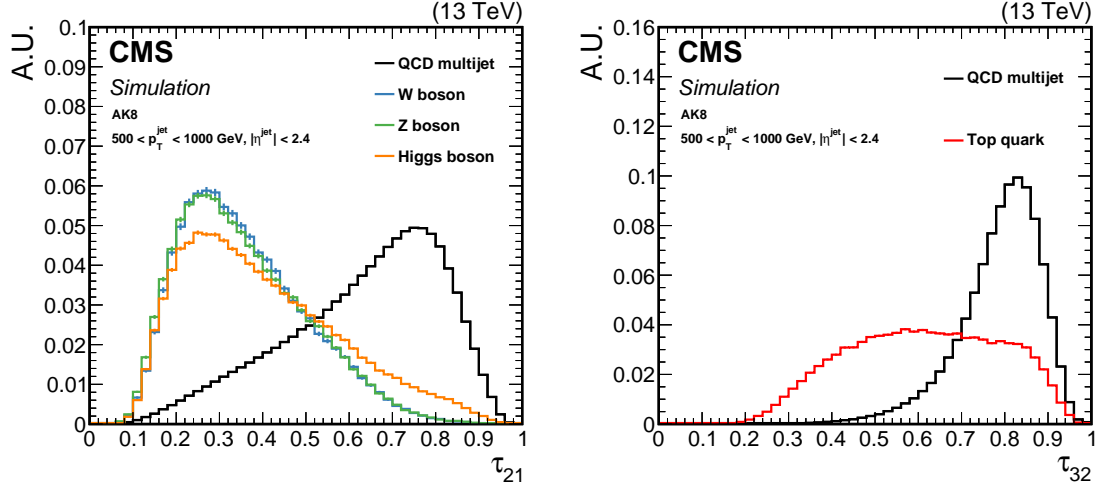


Figure 3.1: Comparison of τ_{21} and τ_{32} shapes for signal and background in AK8 jets. The left is τ_{21} distribution showing discrimination W/Z/H jets vs QCD jet, and the right is τ_{32} distribution for t-quark vs QCD jets [38].

dissertation where we utilize mass regions of fatjet to normalize background contribution.

Figure 3.2 describes the architecture of ‘‘DeepAK8’’ tagging.

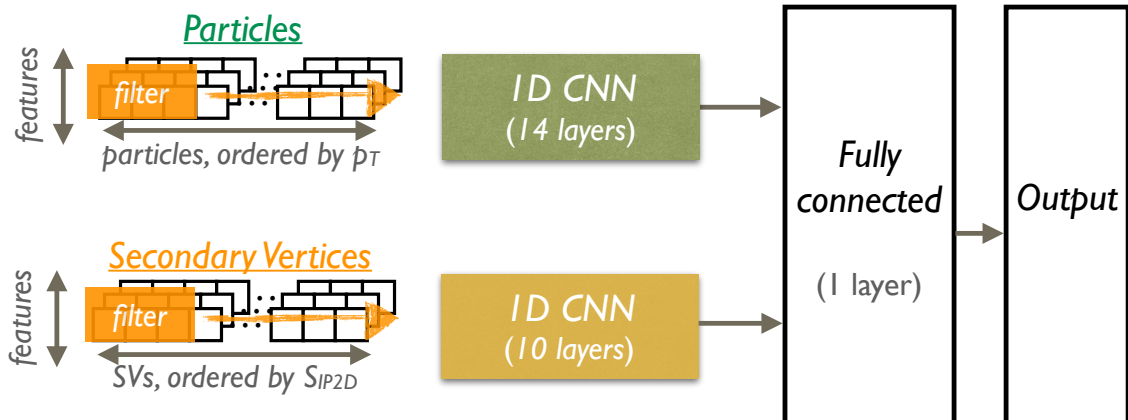


Figure 3.2: The network architecture of DeepAK8 [38]

3.2.3.2 Softdrop Mass

Fatjets can also have contamination coming from wide angle soft initial state radiation (ISR) and multiple hadron scattering, which affects the mass calculation of the jet, to remove such contamination and have better mass reconstruction, the “softdrop” mass algorithm [39] is used.

Softdrop is a declustering algorithm which removes the particle from the jet with radius R_0 , when the following condition between two particles is satisfied,

$$\frac{\min(p_{T,1}, p_{T,2})}{p_{T,1} + p_{T,2}} > z_{cut} \left(\frac{\Delta R_{12}}{R_0} \right)^\beta \quad (3.7)$$

where ΔR_{12} is the distance between the two particles, z_{cut} and β are the parameters for tuning softdrop declustering. For fatjets used in CMS, they have softdrop applied with $\beta = 0$ and $z_{cut} = 0.1$ which vetoes both soft and soft-collinear emissions in a jet.

3.2.4 Missing transverse momentum

Invisible particles like neutrinos cannot be detected at CMS directly. Kinematics of such particles can be determined using laws of conservation of total momentum. In case of proton-proton collision, the actual collision happens between quarks contained in proton and quarks carry fraction of proton momentum and can not be determined exactly, for this reasons kinematic determination of invisible particles is limited to transverse plane only.

After all the particles are reconstructed in an event, their p_T 's can be used to determine missing transverse momentum as,

$$\vec{p}_T^{miss} = - \sum \vec{p}_T \quad (3.8)$$

It's usually neutrinos which contributes to missing transverse momentum, and they have very small mass, the missing transverse momentum is then equivalent to Missing Transverse Energy (MET), which is most often used term in physics analysis.

3.3 TBD Monte Carlo Simulation

3.3.1 TBD Generators

3.3.2 TBD Hadronization

CHAPTER 4

VBS MEASUREMENT IN ZVJJ FINAL STATE

As discussed in Section 1.2 this analysis targets VBS of ZV with two jets in final state. The goal of the analysis is to reduce contribution from background processes as much as possible without loosing much of signal, and measure signal strength and significance.

Since Z decays leptonically and V is decaying hadronically, the phase-space of this analysis can be either l^+l^-jjjj or l^+l^-Jjj , where l are leptons, j are narrow jets and J is a boosted (wider) jet. The phase-space is divided into two broad regions signal and controlled, signal region is constructed based on theory such that it is mostly signal process and controlled region is basically orthogonal to the signal region where we expect contributions mostly from background processes.

The analysis is performed “blind” to avoid intrinsic bias i.e. until the analysis procedure is finalized, the collision data is only used in controlled regions. Once the analysis technique is optimized using MC samples and validated against collision data in controlled regions. Once the analysis technique is satisfactory and approved by CMS Physics Group then the results are “un-blinded” i.e. measurements are done using collision data in signal region.

4.1 TBD Signal and Background

4.2 Dataset and Simulation

The analysis uses NANOAOD v7 tier of datasets provided centrally by CMS collaboration.

4.2.1 Data

The Table 4.1 contains the list of HLT Trigger paths used in this analysis.

4.2.2 MC Simulations

The Table 4.2, 4.3, 4.4 contains the list of Signal and Background MC samples used for modeling in this analysis.

Table 4.1: Trigger paths used to select events in CMS collision data

Dataset	Year	HLT Path
Single Muon	2016	HLT_IsoMu24 HLT_IsoTkMu24
	2017	HLT_IsoMu27
	2018	HLT_IsoMu24
Single Electron	2016	HLT_Ele27_WPTight_Gsf HLT_Ele25_eta2p1_WPTight_Gsf
	2017	HLT_Ele35_WPTight_Gsf
	2018	HLT_Ele32_WPTight_Gsf
Double Muon	2016	HLT_Mu17_TrkIsoVVL_Mu8_TrkIsoVVL_DZ HLT_Mu17_TrkIsoVVL_TkMu8_TrkIsoVVL_DZ HLT_TkMu17_TrkIsoVVL_TkMu8_TrkIsoVVL_DZ
	2017	HLT_Mu17_TrkIsoVVL_Mu8_TrkIsoVVL_DZ_Mass8 HLT_Mu17_TrkIsoVVL_Mu8_TrkIsoVVL_DZ_Mass3p8
	2018	HLT_Mu17_TrkIsoVVL_Mu8_TrkIsoVVL_DZ_Mass3p8
	2016	HLT_Ele23_Ele12_CaloIdL_TrackIdL_IsoVL_DZ HLT_Ele23_Ele12_CaloIdL_TrackIdL_IsoVL
Double Electron	2017	HLT_Ele23_Ele12_CaloIdL_TrackIdL_IsoVL
	2018	HLT_Ele23_Ele12_CaloIdL_TrackIdL_IsoVL

Table 4.2: List of MC samples for Signal and Background modeling

Process	Year	Cross Section (pb)
VBS_EWK (Signal)	2016	WminusTo2JZTo2LJJ_EWK_LO_SM_MJJ100PTJ10_TuneCUETP8M1_13TeV-madgraph-pythia8
	2016	WplusTo2JZTo2LJJ_EWK_LO_SM_MJJ100PTJ10_TuneCUETP8M1_13TeV-madgraph-pythia8
	2016	ZTo2LZTo2JJ_EWK_LO_SM_MJJ100PTJ10_TuneCUETP8M1_13TeV-madgraph-pythia8
	2017, 2018	WminusTo2JZTo2LJJ_EWK_LO_SM_MJJ100PTJ10_TuneCP5_13TeV-madgraph-pythia8
	2017, 2018	WplusTo2JZTo2LJJ_EWK_LO_SM_MJJ100PTJ10_TuneCP5_13TeV-madgraph-pythia8
	2017, 2018	ZTo2LZTo2JJ_EWK_LO_SM_MJJ100PTJ10_TuneCP5_13TeV-madgraph-pythia8
	2016	WminusTo2JZTo2LJJ_QCD_LO_SM_MJJ100PTJ10_TuneCUETP8M1_13TeV-madgraph-pythia8
	2016	WplusTo2JZTo2LJJ_QCD_LO_SM_MJJ100PTJ10_TuneCUETP8M1_13TeV-madgraph-pythia8
	2016	ZTo2LZTo2JJ_QCD_LO_SM_MJJ100PTJ10_TuneCUETP8M1_13TeV-madgraph-pythia8
	2017, 2018	WminusTo2JZTo2LJJ_QCD_LO_SM_MJJ100PTJ10_TuneCP5_13TeV-madgraph-pythia8
VBS_QCD (Background)	2017, 2018	WplusTo2JZTo2LJJ_QCD_LO_SM_MJJ100PTJ10_TuneCP5_13TeV-madgraph-pythia8
	2017, 2018	ZTo2LZTo2JJ_QCD_LO_SM_MJJ100PTJ10_TuneCP5_13TeV-madgraph-pythia8
	2017, 2018	DYJetsToLL_M-50_HT-70to100_TuneCUETP8M1_13TeV-madgraphMLM-pythia8
	2016	DYJetsToLL_M-50_HT-100to200_TuneCUETP8M1_13TeV-madgraphMLM-pythia8
	2016	DYJetsToLL_M-50_HT-200to400_TuneCUETP8M1_13TeV-madgraphMLM-pythia8
DY + Jets LO (Background)	2016	DYJetsToLL_M-50_HT-400to600_TuneCUETP8M1_13TeV-madgraphMLM-pythia8
	2016	DYJetsToLL_M-50_HT-600to800_TuneCUETP8M1_13TeV-madgraphMLM-pythia8
	2016	DYJetsToLL_M-50_HT-800to1200_TuneCUETP8M1_13TeV-madgraphMLM-pythia8
	2016	DYJetsToLL_M-50_HT-1200to2500_TuneCUETP8M1_13TeV-madgraphMLM-pythia8
	2016	DYJetsToLL_M-50_HT-2500toInf_TuneCUETP8M1_13TeV-madgraphMLM-pythia8
	2017	DYJetsToLL_M-50_HT-70to100_TuneCP5_13TeV-madgraphMLM-pythia8
	2017	DYJetsToLL_M-50_HT-100to200_TuneCP5_13TeV-madgraphMLM-pythia8
	2017	DYJetsToLL_M-50_HT-200to400_TuneCP5_13TeV-madgraphMLM-pythia8
	2017	DYJetsToLL_M-50_HT-400to600_TuneCP5_13TeV-madgraphMLM-pythia8
	2017	DYJetsToLL_M-50_HT-600to800_TuneCP5_13TeV-madgraphMLM-pythia8

Table 4.3: List of MC samples for Signal and Background modeling

Process	Year	Dataset Name	Cross Section (pb)
DY + Jets LO (Background)	2018	DYJetsToLL_M-50_HT-70to100_TuneCP5_PSweights_13TeV-madgraphMLM-pythia8	167.33
	2018	DYJetsToLL_M-50_HT-100to200_TuneCP5_PSweights_13TeV-madgraphMLM-pythia8	161.1
	2018	DYJetsToLL_M-50_HT-200to400_TuneCP5_PSweights_13TeV-madgraphMLM-pythia8	48.66
	2018	DYJetsToLL_M-50_HT-400to600_TuneCP5_PSweights_13TeV-madgraphMLM-pythia8	6.968
	2018	DYJetsToLL_M-50_HT-600to800_TuneCP5_PSweights_13TeV-madgraphMLM-pythia8	1.743
	2018	DYJetsToLL_M-50_HT-800to1200_TuneCP5_PSweights_13TeV-madgraphMLM-pythia8	0.8052
	2018	DYJetsToLL_M-50_HT-1200to2500_TuneCP5_PSweights_13TeV-madgraphMLM-pythia8	0.1933
	2018	DYJetsToLL_M-50_HT-2500toInf_TuneCP5_PSweights_13TeV-madgraphMLM-pythia8	0.003468
	2016	ST_tW_antitop_5f_NoFullyHadronicDecays_13TeV_PSweights-powheg-pythia8	38.06
	2016	ST_tW_antitop_5f_inclusiveDecays_TuneCP5_PSweights_13TeV-powheg-pythia8	34.97
Top (Background)	2016	ST_tW_top_5f_NoFullyHadronicDecays_13TeV_PSweights-powheg-pythia8	38.09
	2016	ST_tW_top_5f_inclusiveDecays_TuneCP5_PSweights_13TeV-powheg-pythia8	34.91
	2016	ST_t-channel1_antitop_4f_InclusiveDecays_TuneCP5_PSweights_13TeV-powheg-pythia8	67.91
	2016	ST_t-channel1_top_4f_InclusiveDecays_TuneCP5_PSweights_13TeV-powheg-pythia8	113.3
	2016	ST_s-channel1_4f_leptonDecays_13TeV_PSweights-amcatnlo-pythia8	3.365
	2016	ST_s-channel1_4f_hadronicDecays_TuneCP5_PSweights_13TeV-amcatnlo-pythia8	11.24
	2016	ST_s-channel1_4f_InclusiveDecays_13TeV-amcatnlo-pythia8	10.12
	2016	TTToHadronic_TuneCP5_PSweights_13TeV-powheg-pythia8	377.96
	2016	TTToSemiLeptonic_TuneCP5_PSweights_13TeV-powheg-pythia8	365.34
	2016	TTTo2L2Nu_TuneCP5_PSweights_13TeV-powheg-pythia8	88.29
	2017	TTToSemiLeptonic_TuneCP5_13TeV-powheg-pythia8	365.34
	2017	TTTo2L2Nu_TuneCP5_13TeV-powheg-pythia8	86.99
	2017	TTToHadronic_TuneCP5_13TeV-powheg-pythia8	377.96
	2017	ST_s-channel1_antitop_leptonDecays_13TeV-PSweights_powheg-pythia	1.33
	2017	ST_s-channel1_top_leptonDecays_13TeV-PSweights_powheg-pythia	2.13
	2017	ST_t-channel1_antitop_5f_TuneCP5_PSweights_13TeV-powheg-pythia8	27.19
	2017	ST_t-channel1_top_5f_TuneCP5_13TeV-powheg-pythia8	45.7
	2017	ST_tW_antitop_5f_inclusiveDecays_TuneCP5_13TeV-powheg-pythia8	12.04
	2017	ST_tW_top_5f_inclusiveDecays_TuneCP5_13TeV-powheg-pythia8	12.04

Table 4.4: List of MC samples for Signal and Background modeling

Process	Year	Dataset Name	Cross Section (pb)
Top (Background)	2018	TTToSemileptonic_TuneCP5_13TeV-powheg-pythia8	365.34
	2018	TTTo2L2Nu_TuneCP5_13TeV-powheg-pythia8	86.99
	2018	TTToHadronic_TuneCP5_13TeV-powheg-pythia8	377.96
	2018	ST_s-channel_antitop_leptonDecays_13TeV-PSweights_powheg-pythia	1.33
	2018	ST_s-channel_top_leptonDecays_13TeV-PSweights_powheg-pythia	2.13
	2018	ST_t-channel_antitop_5f_TuneCP5_13TeV-powheg-pythia8	27.19
	2018	ST_t-channel_top_5f_TuneCP5_13TeV-powheg-pythia8	45.7
	2018	ST_tW_DS_antitop_5f_inclusiveDecays_TuneCP5_13TeV-powheg-pythia8	12.04
	2018	ST_tW_DS_top_5f_inclusiveDecays_TuneCP5_13TeV-powheg-pythia8	12.04

4.3 TBD Event Selection

4.3.1 TBD HLT Trigger

4.3.2 TBD Lepton Selection

4.3.2.1 TBD Muon

4.3.2.2 TBD Electron

4.3.3 TBD VBS Tagged Jets

4.3.4 TBD V Jet Candidate

CHAPTER 5

HIGH GRANULARITY CALORIMETER UPGRADE

About High Luminosity LHC (HL-LHC) High Granularity Calorimeter (HGCAL) Upgrade

5.1 Technical Design

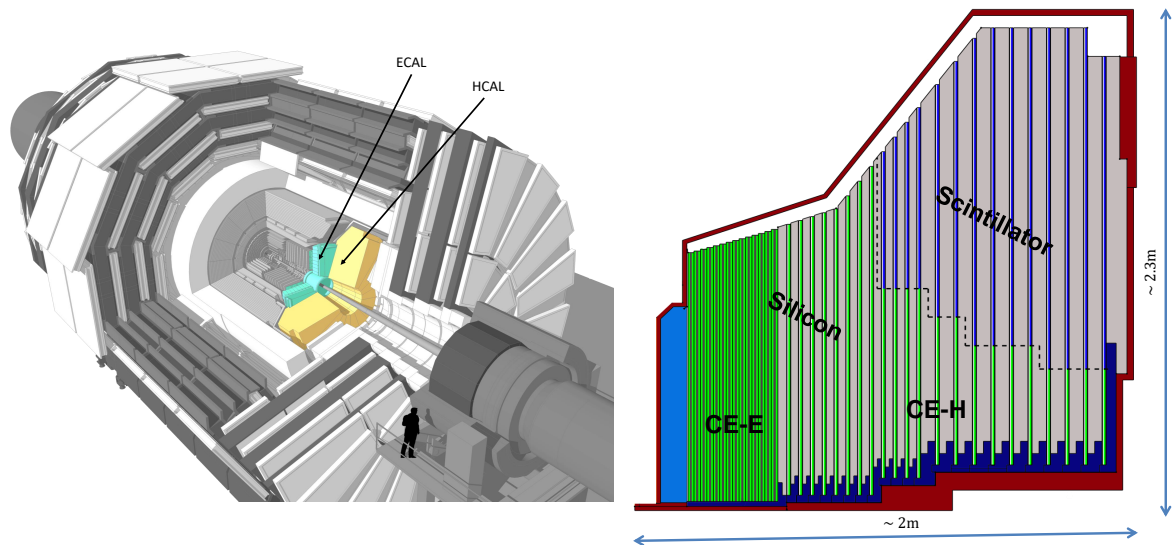


Figure 5.1: Overview of CE [40, 41]

5.2 Scintillator Tiles

5.2.1 End of Life Scenario

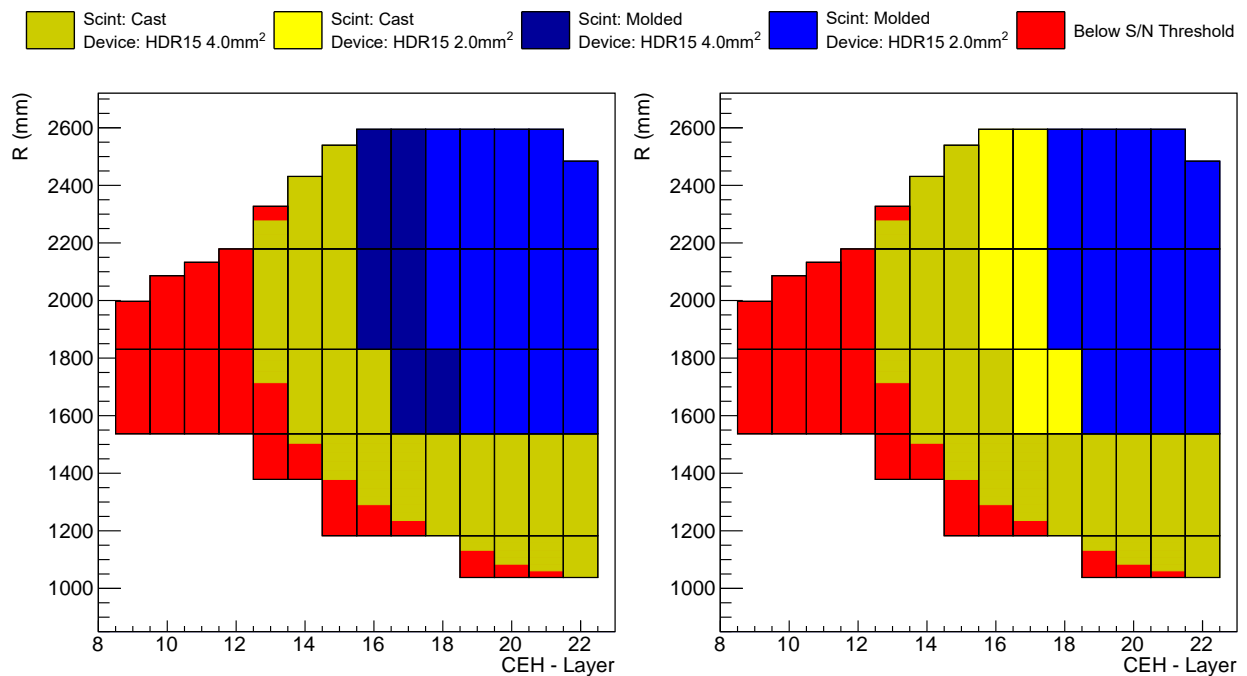


Figure 5.2: HGCAL scenarios

Table 5.1: HGCAL scenarios comparison

		Scene A	Scene B
Cast Scintillator	Cell Count	148, 608	176, 256
	Total Area	185.13 m ²	239.45 m ²
	Percentage	50.6 %	65.5 %
Injection Molded Scintillator	Cell Count	91, 008	63, 360
	Total Area	180.5 m ²	126.18 m ²
	Percentage	49.4 %	34.5 %
SiPMs Count	2 mm ²	63, 360	91, 008
	4 mm ²	100, 224	148, 608

CHAPTER 6

TBD RESULTS

REFERENCES

- [1] Wikipedia contributors. “Standard Model of Elementary Particles” (July 2021). Accessed September 07, 2021. URL: https://en.wikipedia.org/wiki/File:Standard_Model_of_Elementary_Particles.svg.
- [2] C. N. Yang and R. L. Mills. “Conservation of Isotopic Spin and Isotopic Gauge Invariance”. *Phys. Rev.* 96 (1 Oct. 1954), pp. 191–195. DOI: [10.1103/PhysRev.96.191](https://doi.org/10.1103/PhysRev.96.191). URL: <https://link.aps.org/doi/10.1103/PhysRev.96.191>.
- [3] S. L. Glashow. “The renormalizability of vector meson interactions”. *Nuclear Physics* 10 (Feb. 1959), pp. 107–117. DOI: [10.1016/0029-5582\(59\)90196-8](https://doi.org/10.1016/0029-5582(59)90196-8).
- [4] S. Weinberg. “A Model of Leptons”. *Physical Review Letters* 19 (Nov. 1967), pp. 1264–1266. DOI: [10.1103/physrevlett.19.1264](https://doi.org/10.1103/physrevlett.19.1264).
- [5] A. Salam and J. C. Ward. “Weak and electromagnetic interactions”. *Il Nuovo Cimento* 11 (Feb. 1959), pp. 568–577. DOI: [10.1007/bf02726525](https://doi.org/10.1007/bf02726525).
- [6] F. Englert and R. Brout. “Broken Symmetry and the Mass of Gauge Vector Mesons”. *Physical Review Letters* 13 (Aug. 1964), pp. 321–323. DOI: [10.1103/physrevlett.13.321](https://doi.org/10.1103/physrevlett.13.321).
- [7] P. W. Higgs. “Broken Symmetries and the Masses of Gauge Bosons”. *Physical Review Letters* 13 (Oct. 1964), pp. 508–509. DOI: [10.1103/physrevlett.13.508](https://doi.org/10.1103/physrevlett.13.508).
- [8] J. Ellis. “Higgs Physics”. en (2015). DOI: [10.5170/CERN-2015-004.117](https://doi.org/10.5170/CERN-2015-004.117).
- [9] B. W. Lee, C. Quigg, and H. B. Thacker. “Weak interactions at very high energies: The role of the Higgs-boson mass”. *Physical Review D* 16 (Sept. 1977), pp. 1519–1531. DOI: [10.1103/physrevd.16.1519](https://doi.org/10.1103/physrevd.16.1519).

- [10] B. W. Lee, C. Quigg, and H. B. Thacker. “Strength of Weak Interactions at Very High Energies and the Higgs Boson Mass”. *Physical Review Letters* 38 (Apr. 1977), pp. 883–885. DOI: [10.1103/physrevlett.38.883](https://doi.org/10.1103/physrevlett.38.883).
- [11] A. Denner and T. Hahn. “Radiative Corrections to $W^+W^- \rightarrow W^+W^-$ in the Electroweak Standard Model”. *Nucl.Phys.B* 525:27-50, 1998 (Nov. 12, 1997). DOI: [10.1016/S0550-3213\(98\)00287-9](https://doi.org/10.1016/S0550-3213(98)00287-9).
- [12] L. Evans and P. Bryant. “LHC Machine”. *Journal of Instrumentation* 3.08 (Aug. 2008), S08001–S08001. DOI: [10.1088/1748-0221/3/08/s08001](https://doi.org/10.1088/1748-0221/3/08/s08001).
- [13] E. Mobs. “The CERN accelerator complex - 2019” (July 2019). Accessed August 16, 2021. URL: <http://cds.cern.ch/record/2684277/files/>.
- [14] Public CMS Luminosity Information. “Cumulative delivered and recorded luminosity versus time for run-2 pp data” (2018). Accessed August 17, 2021. URL: <https://twiki.cern.ch/twiki/bin/view/CMSPublic/LumiPublicResults>.
- [15] The CMS Collaboration. “CMS Luminosity Measurements for the 2016 Data Taking Period” (2017). URL: <https://cds.cern.ch/record/2257069>.
- [16] The CMS Collaboration. “CMS luminosity measurement for the 2017 data-taking period at $\sqrt{s} = 13$ TeV” (2018). URL: <https://cds.cern.ch/record/2621960>.
- [17] The CMS Collaboration. “CMS luminosity measurement for the 2018 data-taking period at $\sqrt{s} = 13$ TeV” (2019). URL: <https://cds.cern.ch/record/2676164>.
- [18] T. Sakuma. “Cutaway diagrams of CMS detector” (May 2019). Accessed August 17, 2021. URL: <https://cds.cern.ch/record/2665537>.
- [19] The CMS Collaboration. “The CMS experiment at the CERN LHC”. *Journal of Instrumentation* 3.08 (Aug. 2008), S08004–S08004. DOI: [10.1088/1748-0221/3/08/s08004](https://doi.org/10.1088/1748-0221/3/08/s08004). URL: <https://doi.org/10.1088/1748-0221/3/08/s08004>.

- [20] The CMS Collaboration. “CMS Detector Slice” (Jan. 2016). Accessed August 18, 2021. URL: <https://cds.cern.ch/record/2120661>.
- [21] M. Brice and C. Marcelloni. “The central part of CMS is lowered” (Feb. 2007). Accessed August 22, 2021. URL: <https://cds.cern.ch/record/1020311>.
- [22] T. Sakuma. “SketchUp Drawings of the Phase 1 pixel detector alongside the current pixel detector” (June 2012). Accessed August 17, 2021. URL: <https://cms-docdb.cern.ch/cgi-bin/PublicDocDB>ShowDocument?docid=6473>.
- [23] The CMS Collaboration. “The CMS ECAL performance with examples”. *Journal of Instrumentation* 9.02 (Feb. 2014), pp. C02008–C02008. DOI: [10.1088/1748-0221/9/02/c02008](https://doi.org/10.1088/1748-0221/9/02/c02008).
- [24] The CMS Collaboration. “Images of CMS ECAL Endcap (EE)” (Nov. 2008). Accessed August 22, 2021. URL: <https://cds.cern.ch/record/1431479>.
- [25] J. Mans et al. “CMS Technical Design Report for the Phase 1 Upgrade of the Hadron Calorimeter” (Sept. 2012). URL: <https://cds.cern.ch/record/1481837>.
- [26] The CMS Collaboration. “Images of the CMS HCAL Barrel (HB)” (2008). Accessed August 22, 2021. URL: <https://cds.cern.ch/record/1431485>.
- [27] The CMS Collaboration. “HCAL Depth Segmentation Phase 1 Upgrade” (2012). Accessed August 22, 2021. URL: <https://home.fnal.gov/~chlebana/CMS/Phase1>.
- [28] The CMS Collaboration. “Performance of the CMS Muon Detectors in early 2016 collision runs” (2016). Accessed August 22, 2021. URL: <https://twiki.cern.ch/twiki/pub/CMSPublic/MuonDPGPublic160729>.
- [29] The CMS Collaboration. “Particle-flow reconstruction and global event description with the CMS detector”. *Journal of Instrumentation* 12.10 (Oct. 2017), P10003–P10003. DOI: [10.1088/1748-0221/12/10/p10003](https://doi.org/10.1088/1748-0221/12/10/p10003).

- [30] S. Cucciarelli et al. “Track reconstruction, primary vertex finding and seed generation with the Pixel Detector”. CMS-NOTE-2006-026 (Jan. 2006). URL: <https://cds.cern.ch/record/927384>.
- [31] W. Adam et al. “Track Reconstruction in the CMS tracker”. CMS-NOTE-2006-041 (Dec. 2006). URL: <https://cds.cern.ch/record/934067>.
- [32] W. Adam et al. “Reconstruction of electrons with the Gaussian-sum filter in the CMS tracker at the LHC”. *Journal of Physics G: Nuclear and Particle Physics* 31.9 (July 2005), N9–N20. DOI: [10.1088/0954-3899/31/9/n01](https://doi.org/10.1088/0954-3899/31/9/n01).
- [33] The CMS Collaboration. “Electron and photon reconstruction and identification with the CMS experiment at the CERN LHC”. *JINST* 16 (2021) P05014 (Dec. 12, 2020). DOI: [10.1088/1748-0221/16/05/P05014](https://doi.org/10.1088/1748-0221/16/05/P05014).
- [34] M. Cacciari, G. P. Salam, and G. Soyez. “FastJet user manual” (Nov. 25, 2011). DOI: [10.1140/epjc/s10052-012-1896-2](https://doi.org/10.1140/epjc/s10052-012-1896-2).
- [35] D. Bertolini et al. “Pileup Per Particle Identification”. *JHEP* 1410 (2014) 59 (July 22, 2014). DOI: [10.1007/JHEP10\(2014\)059](https://doi.org/10.1007/JHEP10(2014)059).
- [36] The CMS Collaboration. “Pileup mitigation at CMS in 13 TeV data”. *Journal of Instrumentation* 15.09 (Sept. 2020), P09018–P09018. DOI: [10.1088/1748-0221/15/09/p09018](https://doi.org/10.1088/1748-0221/15/09/p09018).
- [37] J. Thaler and K. V. Tilburg. “Identifying Boosted Objects with N-subjettiness”. *JHEP* 1103:015, 2011 (Nov. 10, 2010). DOI: [10.1007/JHEP03\(2011\)015](https://doi.org/10.1007/JHEP03(2011)015).
- [38] The CMS Collaboration. “Identification of heavy, energetic, hadronically decaying particles using machine-learning techniques”. *JINST* 15 (2020) P06005 (Apr. 17, 2020). DOI: [10.1088/1748-0221/15/06/P06005](https://doi.org/10.1088/1748-0221/15/06/P06005).

- [39] A. J. Larkoski et al. “Soft Drop”. *JHEP* **1405** (2014) 146 (Feb. 11, 2014). DOI: 10.1007/JHEP05(2014)146.
- [40] D. Barney. “Overview slide of CE with main parameters” (Oct. 2019). Accessed August 24, 2021. URL: <https://cms-docdb.cern.ch/cgi-bin/PublicDocDB>ShowDocument?docid=13251>.
- [41] D. Barney and T. Sakuma. “Sketchup images highlighting the sub-detectors” (Sept. 2017). Accessed August 24, 2021. URL: <https://cds.cern.ch/record/2628519>.

APPENDIX A

MACHINE LEARNING

Write about ML, MVA, Boosted decision tree (BDT), etc.

APPENDIX B

DATA ANALYSIS

Data Analysis Code and Stuff